

STUDY OF MIXED BOUNDARY RECTANGULAR MICROSTRIP ANTENNAS

DR. A. D.

**A Thesis Submitted
In Partial Fulfilment of the Requirements
for the Degree of
MASTER OF TECHNOLOGY**

By
H. V. SREEKANTASWAMY

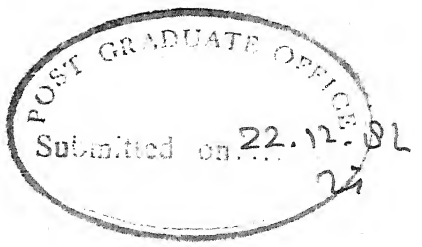
to the

**DEPARTMENT OF ELECTRICAL ENGINEERING
INDIAN INSTITUTE OF TECHNOLOGY, KANPUR
DECEMBER, 1982**

4 JUN 1984

CENTRAL LIBRARY

Ref. No. A.....82690...



CERTIFICATE

This is to certify that the work reported in this thesis entitled 'STUDY OF MIXED BOUNDARY RECTANGULAR MICROSTRIP ANTENNAS' by H.V. Sreekanthaswamy has been carried out under my supervision and has not been submitted elsewhere for a degree.

R. Raghuram
(R. Raghuram)
Assistant Professor
Department of Electrical Engineering
Indian Institute of Technology
Kanpur 208016, India.

ACKNOWLEDGEMENTS

It is with deep sense of gratitude that I express my indebtedness to Drs. K.C. Gupta and R. Raghuram for their exemplary guidance and encouragement.

I extend my sincere and heartfelt thanks to all my friends for providing me with splendid company and for their help and moral support during the course of this work. Mr. and Mrs. H.S. Ningappa, M/s. Girish Kumar, PG Poonacha, AR Shalu and Eswarappa deserve special word of mention.

I express my sincere thanks to Mr. C.M. Abraham for the efficient typing and painstaking efforts in bringing this thesis to its present form.

H.V. Sreekanthaswamy

ABSTRACT

These investigations are aimed at studying the performances of various mixed boundary rectangular microstrip antennas as compared to open-boundary rectangular antennas. Green's function approach with segmentation method has been used for analyzing these antennas. Green's functions for these mixed boundary rectangular segments are derived using the method of images. Green's functions for mixed boundary right-angled isosceles triangular segments are also derived. A comparative study of bandwidth and radiation patterns of these mixed boundary rectangular microstrip antennas with an open-boundary rectangular antenna is carried out. Experimental study of mutual coupling between one-side shorted rectangular antennas is also done.

TABLE OF CONTENTS

	Page
Chapter One INTRODUCTION	1
1.1 TWO-DIMENSIONAL PLANAR COMPONENTS	1
1.1.1 Methods of analysis	1
1.1.2 Applications	4
1.2 MICROSTRIP ANTENNAS	5
1.2.1 Methods of analysis	8
1.2.2 Applications	9
1.3 PRESENT INVESTIGATIONS	9
Chapter Two ANALYSIS OF TWO-DIMENSIONAL COMPONENTS AND GREEN'S FUNCTIONS FOR MIXED BOUNDARY PLANAR SEGMENTS	11
2.1 ANALYSIS USING GREEN'S FUNCTIONS	11
2.1.1 Basic concepts	11
2.1.2 Green's function approach	17
2.2 GREEN'S FUNCTIONS FOR MIXED BOUNDARY PLANAR SEGMENTS	22
2.2.1 Method of images	23
2.2.2 Green's functions for mixed boundary rectangular segments	24
2.2.3 Green's functions for mixed boundary isosceles right-angled triangular segments	33
2.3 DISCUSSION	40

	Page
Chapter Three	
MIXED BOUNDARY RECTANGULAR MICROSTRIP ANTENNAS	41
3.1	41
3.1.1 Green's function approach	41
3.1.2 Segmentation method	44
3.1.3 Radiation pattern calculations	47
3.2	RECTANGULAR PATCH ANTENNA WITH OPEN- BOUNDARY
3.2.1 Analysis	50
3.2.2 Bandwidth	53
3.2.3 Radiation pattern	53
3.3	RECTANGULAR PATCH ANTENNA WITH ONE SIDE AS ELECTRIC WALL
3.3.1 Analysis	54
3.3.2 Bandwidth	57
3.3.3 Radiation pattern	59
3.4	RECTANGULAR PATCH ANTENNA WITH TWO ADJACENT SIDES AS ELECTRIC WALLS
3.4.1 Analysis	61
3.4.2 Bandwidth	63
3.4.3 Radiation pattern	63
3.5	RECTANGULAR PATCH ANTENNA WITH THREE SIDES AS ELECTRIC WALLS
3.5.1 Analysis	65
3.5.2 Bandwidth	67
3.5.3 Radiation pattern	67

	Page
3.6 MEASUREMENT OF MUTUAL COUPLING BETWEEN ONE-SIDE SHORTED RECTANGULAR MICROSTRIP ANTENNAS	69
3.6.1 Introduction	69
3.6.2 Experimental technique and results	71
Chapter Four CONCLUDING REMARKS	75
4.1 SUMMARY OF RESULTS	75
4.2 SUGGESTIONS FOR FURTHER INVESTIGATIONS	76
REFERENCES	78

Chapter One

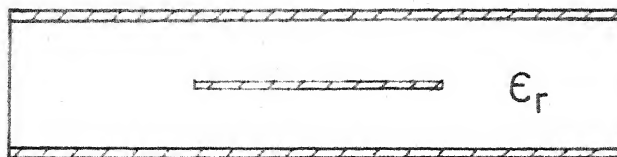
INTRODUCTION

1.1 TWO-DIMENSIONAL PLANAR COMPONENTS

Two-dimensional (2-d) microwave planar components have been proposed for use in microwave integrated circuits [1] - [3]. These components have dimensions comparable to (or greater than) the wavelength in two directions but have the third dimension much smaller than the wavelength. The three types of possible configurations of 2-d components are - (i) triplate or stripline type shown in Figs. 1.1(a) and (c); (ii) open or microstrip type shown in Figs. 1.1(b) and (c); and (iii) waveguide or cavity type shown in Fig. 1.1(d). The triplate and the open type configurations can be considered as generalizations of one-dimensional stripline and microstrip circuits, when the transverse dimensions are comparable to the wavelength. The waveguide type configuration is a special case of three-dimensional waveguide in which the height is much smaller than the wavelength.

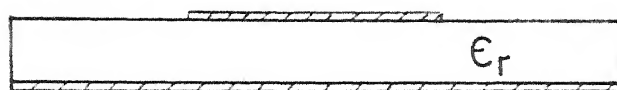
1.1.1 Methods of analysis

There are various methods for obtaining the characterization of 2-d planar components. The choice of the method depends upon the geometry of the 2-d component (i.e. shape of the central conducting patch in a triplate structure or the upper conductor patch in microstrip type circuit).



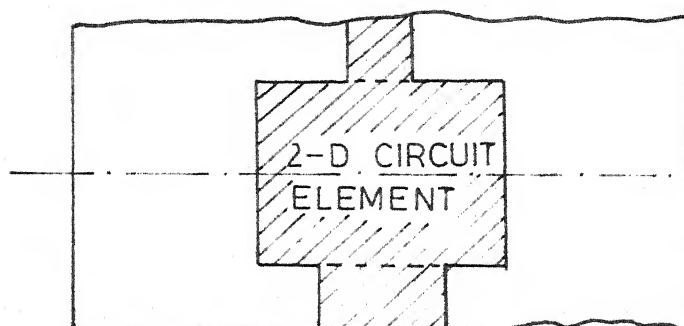
Stripline type

(a)



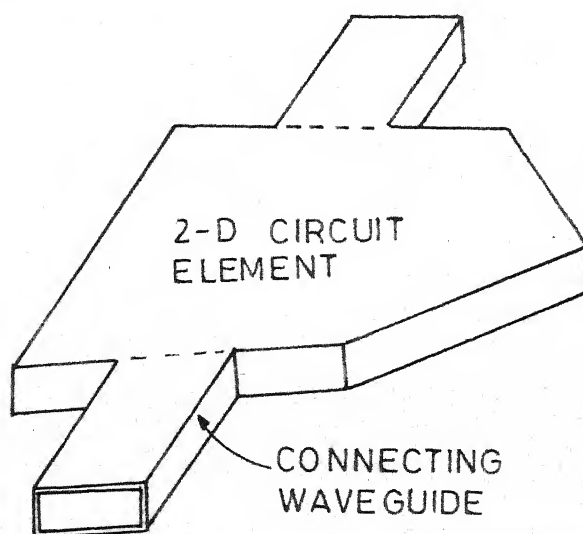
Microstrip type

(b)



Plan view of
(a) and (b)

(c)



Waveguide type

(d)

Fig.1.1 Three types of 2-d microwave circuits

When a 2-d component is of simple geometrical shape, the impedance Green's function [1] technique is the most appropriate method. Green's functions for shapes such as rectangular [2], circular [4], triangular [5], annular ring and sector [6] are available. The impedance matrix of 2-d components with specified locations of ports can be found using these Green's functions.

When the geometrical shape of a 2-d circuit can be considered to be made up of simpler shapes for which the Green's functions are available, the segmentation method [2], [3] can be used for evaluating the characteristics of the overall circuit from those of the various components (of simple shapes). When the shape of a 2-d circuit can be visualised as a regular (simple) shape from which another regular shape has been removed, desegmentation method [7] can be used.

Numerical methods are used for the analysis of arbitrary shaped 2-d components. Finite element approach [8] and contour integral approach [1] have been discussed in the literature. The finite element approach is an extension of finite element methods and involves the integration of certain basis functions over the entire conducting patch which is divided into numerous subsections. The contour integral method is based on the Green's theorem in cylindrical coordinates. The voltage at a point on periphery is

expressed in terms of the line integral along the periphery. The periphery is divided into various sections and the impedance matrix is evaluated at these sections.

1.1.2 Applications

2-d planar components have found several applications in microwave integrated circuits, waveguide circuits, ferrite components and microstrip antennas. Some of the areas where the 2-d approach has found applications are listed below.

- i) Resonators : Two-dimensional components can be used for the design of high-Q resonators used at microwave frequencies. Triangular elements have been proposed for realizing resonators and prototype elements for band-pass and band-stop filters.
- ii) Discontinuity Analysis : The 2-d approach can be employed for the analysis of stripline and microstrip line discontinuities [9] even if equivalent circuits are not available.
- iii) Design of Non-reciprocal Elements : 2-d circuits fabricated on ferrite substrates, may also be analyzed by the 2-d approach using the extension of analysis techniques for circuits on dielectric substrates.
- iv) Microstrip Antennas : Field distribution along the periphery of microstrip antennas can be evaluated by

treating them as 2-d components with magnetic walls.

The 2-d approach can be used to evaluate the voltages at various points along the periphery. The radiation field of these antennas can consequently be calculated from the voltage distribution [10].

1.2 MICROSTRIP ANTENNAS

Microstrip antennas are characterized by more physical parameters than are conventional microwave antennas. They may be of any geometrical shape and any dimension. However, all microstrip antennas can be divided into three basic categories : microstrip patch antennas, microstrip travelling wave antennas and microstrip slot antennas [11].

A simple microstrip patch antenna as shown in Fig. 1.2 consists of a conducting patch of any planar geometry on one side of a dielectric substrate ($\epsilon_r \leq 10$) backed by a ground plane on the other side. In this thesis, investigations are confined to two-dimensional microstrip patch antennas. 2-d microstrip patch antennas employ 2-d planar resonator structures. The successful operation of the high-Q microstrip resonators seems to suggest that basically they are poor radiators. But, microstrip patch antennas have several advantages compared to conventional microwave antennas and therefore have many applications over the broad frequency range of 100 MHz to 50 GHz. The principal advantages are :

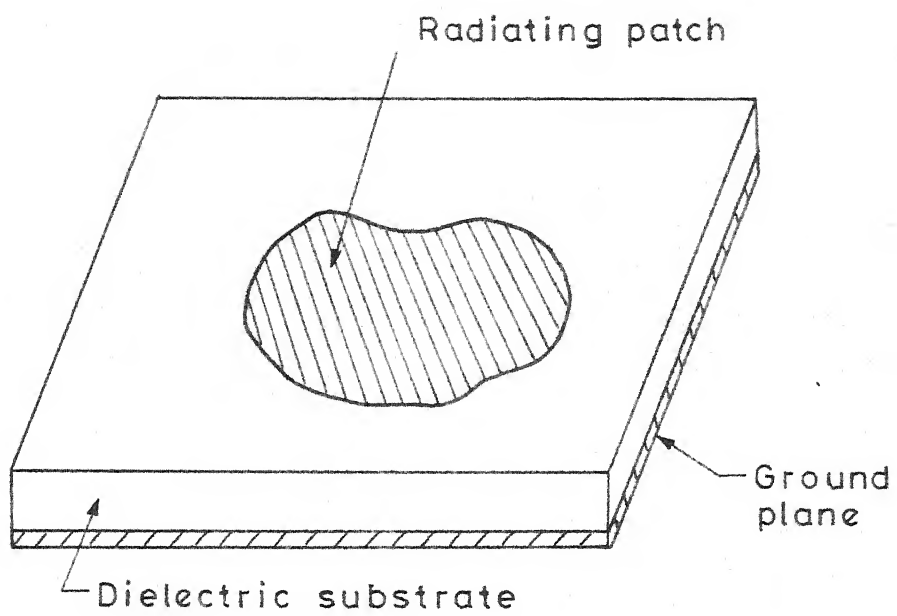


Fig.1.2 Microstrip antenna configuration

- i) light weight, low volume, low profile planar configurations which can be made conformal,
- ii) low fabrication cost; easily amenable to mass production,
- iii) the antennas can be made paper thin and therefore can be easily mounted on missiles, rockets and satellites without major alterations,
- iv) dual frequency antennas can be easily designed,
- v) no cavity backing is required,
- vi) both linear and circular polarization are obtainable,
- vii) microstrip antennas are compatible with modular designs. Solid state devices such as oscillators, amplifiers, variable attenuators, switches, modulators, mixers, phase shifters, etc. can be added directly to the antenna substrate board,
- viii) feed lines and matching networks are fabricated simultaneously with the antenna structure.

The two main disadvantages of microstrip antennas are their relatively narrow bandwidth and excitation of surface waves which propagate along the surface of the dielectric substrate used for antenna. These surface waves can cause radiation in undesired directions and produce excessive mutual coupling between elements in antenna arrays.

1.2.1 Methods of analysis

Several methods for analyzing microstrip patch antennas have been proposed in the literature. Some of these methods are suitable only for the antennas with simple geometries, whereas, others (the numerical methods) have been used for analyzing antennas with complicated geometries. The methods used for the analysis of 2-d components can also be used for 2-d microstrip antennas.

Transmission-line method [12] is the simplest of all the methods, but it is applicable only to rectangular patch antennas. In this technique, the patch antenna is modelled as a transmission line with no transverse field variation. The radiating edges are considered as narrow slots radiating into half space. The effective length of the rectangle after taking into account the open-end fringing fields, is chosen equal to half of the wavelength. The radiation characteristics are obtained by considering the field distribution along the radiating edges to be uniform.

In the modal-expansion method [13], the radiating patch is considered as a resonator with magnetic walls. The field in the cavity is expanded in series of corresponding eigenfunctions. The effect of radiation and other losses is represented in terms of either increased effective loss tangent or by employing impedance boundary condition at the walls.

Green's function approach is used for the analysis of 2-d microstrip patch antennas of simple shapes. Details of the Green's function approach and segmentation method used for analysis of antennas in this thesis are described in Chapter Three.

For the analysis of arbitrary shaped planar antennas, numerical methods such as finite element method [14] and method of moments [15] are available.

1.2.2 Applications

As the advantages of microstrip antennas far outweigh their disadvantages, microstrip antennas have been developed for several applications, e.g., satellite communication, doppler radars, altimeters, missile telemetry, weapon fusing, satellite navigation receivers, phased array radars, biomedical resonators, etc.

1.3 PRESENT INVESTIGATIONS

The antenna element size and mutual coupling between the elements will be less in the case of mixed boundary (both electric and magnetic walls) microstrip antennas compared to open-boundary (i.e., magnetic wall) microstrip antennas. Motivated by this idea, a performance study of various types of mixed boundary rectangular microstrip antennas in terms of bandwidth, radiation pattern and mutual coupling is carried out in this thesis.

Green's functions for rectangular, triangular, circular and sectoral segments with open-boundary are available. Green's functions for rectangular and right-angled isosceles triangular segments with mixed boundary are developed in Chapter Two. Method of images has been used in deriving these Green's functions.

In Chapter Three, various types of mixed boundary rectangular microstrip antennas are analyzed. Green's function technique is used for analyzing these antennas. Green's functions derived in Chapter Two are made use of. Bandwidth and radiation patterns obtained in each case, from theoretical and experimental considerations are discussed. Experimental study of mutual coupling between one-side shorted rectangular antennas is also carried out.

Chapter Four summarises the results and gives suggestions for further investigations in this direction.

Chapter Two

ANALYSIS OF TWO-DIMENSIONAL COMPONENTS AND GREEN'S FUNCTIONS FOR MIXED BOUNDARY PLANAR SEGMENTS

In this chapter, a review of the Green's function approach [1] for the analysis of two-dimensional planar circuits is presented and Green's functions are obtained for mixed boundary rectangular and isosceles right-angled triangular segments.

2.1 ANALYSIS USING GREEN'S FUNCTIONS

2.1.1 Basic concepts

Consider a two-dimensional planar circuit shown in Fig. 2.1. An arbitrary shaped thin conductor is sandwiched midway between two ground conductors spaced $2d$ apart. There are several ports along the periphery. Widths of these ports are denoted as $W_i, W_j \dots$ The rest of the periphery is open-circuited. The coordinate axes are chosen such that the central conductor lies in x - y plane and is perpendicular to the z -axis. Thus, while the dimensions along x and y coordinates are comparable to (or greater than) the wavelength, the thickness along the z -direction is negligible. Therefore, the fields can be assumed to be constant along the z -direction.

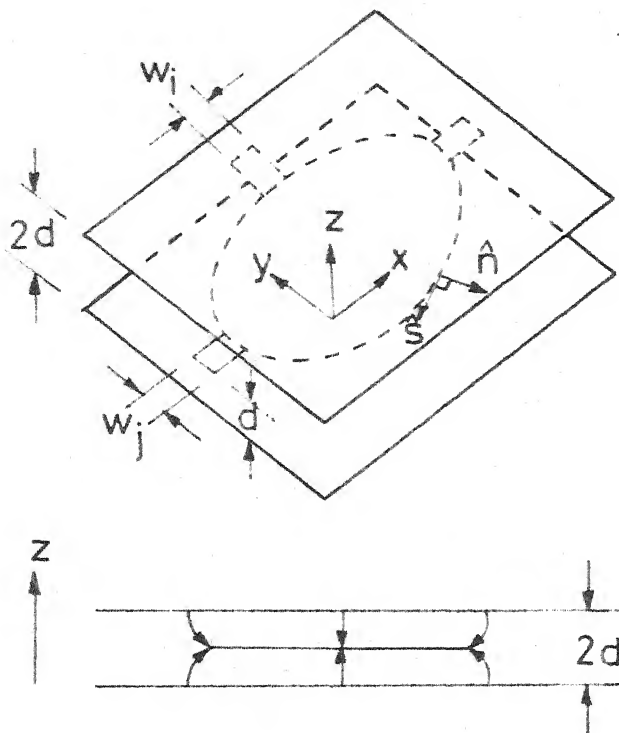


Fig.2.1 Configuration of a stripline type planar circuit

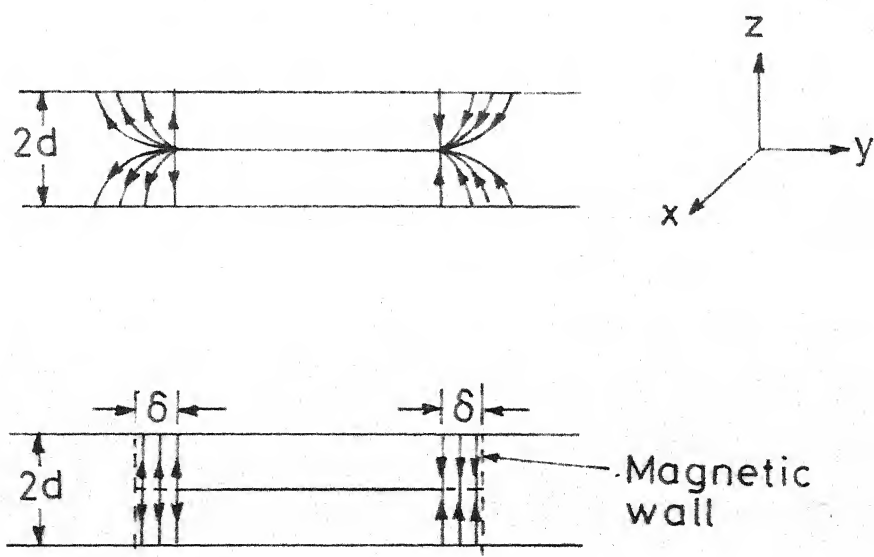


Fig.2.2 Shift in the magnetic wall to account for the fringing field

The general Helmholtz equation, valid for a source free region is given as

$$(\nabla^2 + k^2) \underline{E} = 0, \quad k^2 = \omega^2 \mu \epsilon \quad (2.1)$$

where μ and ϵ denote the permeability and permittivity of the dielectric material and ω is the angular frequency. The above relation holds good for describing the field within the dielectric. At the center conductor and at the ground planes the tangential components of the electric field are zero. A magnetic wall is assumed to exist at the periphery of the 2-d component. Since there is no field variation along the z-direction, both E_x and E_y are equal to zero within the dielectric region. The fringing field at the periphery is taken into account by shifting the magnetic wall by a distance δ from the physical periphery as shown in Fig. 2.2. For stripline type planar circuits, the shift δ is given by [16]

$$\delta = \frac{2d \ln 2}{\pi} \quad (2.2)$$

This value of δ is exact for a semi-infinite patch only, but it can be used in most practical cases. For microstrip type circuits, the value of δ is found from the expression for the fringing capacitance at an open-ended microstrip [9].

It may be noted that the fields above and below the central patch must be oppositely directed. In the

following discussions, the \underline{E} and \underline{H} can be taken to be the fields on one side of the central patch, say the lower side.

Since both E_x and E_y are zero, the E -field may be written as

$$\underline{E} = \hat{a}_z E_z(x, y) \quad (2.3)$$

where \hat{a}_z is a unit vector along the z -direction and E_z is a function of x and y coordinates only. Substituting (2.3) in (2.1) and putting $\frac{\partial E_z}{\partial z}$ equal to zero, one gets

$$(\nabla_T^2 + k^2) E_z = 0 \quad (2.4)$$

where $\nabla_T^2 = \frac{\partial^2}{\partial x^2} + \frac{\partial^2}{\partial y^2}$. Using Maxwell's equation, the magnetic field can be written as

$$\underline{H} = - \frac{1}{j\omega\mu} \nabla \times \underline{E} \quad (2.5)$$

Using (2.3), this reduces to

$$\underline{H} = \frac{1}{j\omega\mu} \left(- \frac{\partial E_z}{\partial y} \hat{a}_x + \frac{\partial E_z}{\partial x} \hat{a}_y \right) \quad (2.6)$$

Surface current on a conducting sheet can be obtained from the boundary condition

$$\underline{J}_s = \hat{n} \times (\underline{H}_1 - \underline{H}_2) \quad (2.7)$$

where \hat{n} is a unit vector normal to the boundary and \underline{H}_1 and \underline{H}_2 are magnetic fields on the two sides of a conducting sheet. For the central conductor of a stripline type

2-d circuit, $\underline{H}_1 = -\underline{H}_2$ and hence

$$\underline{J}_s = \frac{2}{j\omega\mu} \left(\frac{\partial E_z}{\partial x} \hat{a}_x + \frac{\partial E_z}{\partial y} \hat{a}_y \right) \text{ amps/m} \quad (2.8)$$

For microstrip type 2-d circuits (after the periphery has been extended to account for the fringing fields), there will be no magnetic field above the upper conducting plane and so the factor of 2 in (2.8) will not appear for obtaining the surface current on the conducting patch.

The expression for \underline{J}_s in (2.8) is valid at all points on the central patch including the periphery. For points on the periphery, \underline{J}_s can be rewritten in terms of components which are tangential and normal to the periphery as

$$\underline{J}_s = \frac{2}{j\omega\mu} \left(\frac{\partial E_z}{\partial s} \hat{s} + \frac{\partial E_z}{\partial n} \hat{n} \right) \text{ amps/m} \quad (2.9)$$

where \hat{s} and \hat{n} are unit vectors tangential and normal to the periphery as shown in Fig. 2.1. For points on the periphery where there are no coupling ports, the normal component of the surface current must be zero, i.e.

$$\frac{\partial E_z}{\partial n} = 0 \quad (2.10)$$

At a coupling port on the periphery, the planar circuit can be excited by a stripline (or microstrip) and the current flow (at the coupling port) is normal to the periphery. This current is obtained using (2.9) as

$$i = - \int_W \left(\frac{2}{j\omega\mu} \frac{\partial E_z}{\partial n} \right) ds \quad (2.11)$$

where W is the width of the coupling port and ds is the incremental distance along the periphery. The negative sign appears in (2.11) because the current i flows inwards whereas \hat{n} in (2.9) points outwards.

The characterization of the planar components can be carried out in terms of an RF voltage V on the central conductor. Since $\partial E_z / \partial z = 0$, V is obtained from (2.3) as

$$V = -E_z d \quad (2.12)$$

Equations (2.4), (2.10) and (2.11) can now be written as follows :

$$(\nabla_T^2 + k^2)V = 0 \quad (2.13)$$

With

$$\frac{\partial V}{\partial n} = 0 \quad (2.14)$$

for points on the periphery where there are no coupling ports. The current flowing in at a coupling port is expressed as

$$i = \frac{2}{j\omega\mu d} \int_W \frac{\partial V}{\partial n} ds \quad (2.15)$$

Solution to (2.13), with (2.14) and (2.15) as the boundary conditions, leads to the characterization of stripline type of planar circuits. For microstrip type planar circuits,

the boundary condition (2.15) is modified so that the factor of 2 on the right-hand side does not appear.

2.1.2 Green's function approach

This approach can be employed when the shape of the 2-d patch is relatively simple. The Green's function, which gives voltage at any point for a unit source current excitation elsewhere, is obtained analytically. When the locations of the ports are specified, the impedance matrix of the component can be easily derived using the Green's function.

A. Source currents

If a planar component is excited by a current density J_z in z-direction at any arbitrary point (x_0, y_0) inside the periphery as shown in Fig. 2.3, the wave equation can be written as

$$(\nabla_T^2 + k^2) V = -j\omega\mu dJ_z \quad (2.16)$$

When the circuit is excited by a stripline, J_z denotes a fictitious RF current density injected normally into the circuit. It may be noted that the line current density ($J_n = \frac{2}{j\omega\mu d} \frac{\partial V}{\partial n}$), being injected into the circuit at coupling ports located on the periphery, can equivalently be considered as fed normal to the circuit (along the z-direction) with the magnetic wall condition $\frac{\partial V}{\partial n} = 0$ imposed all along the periphery. This can be explained

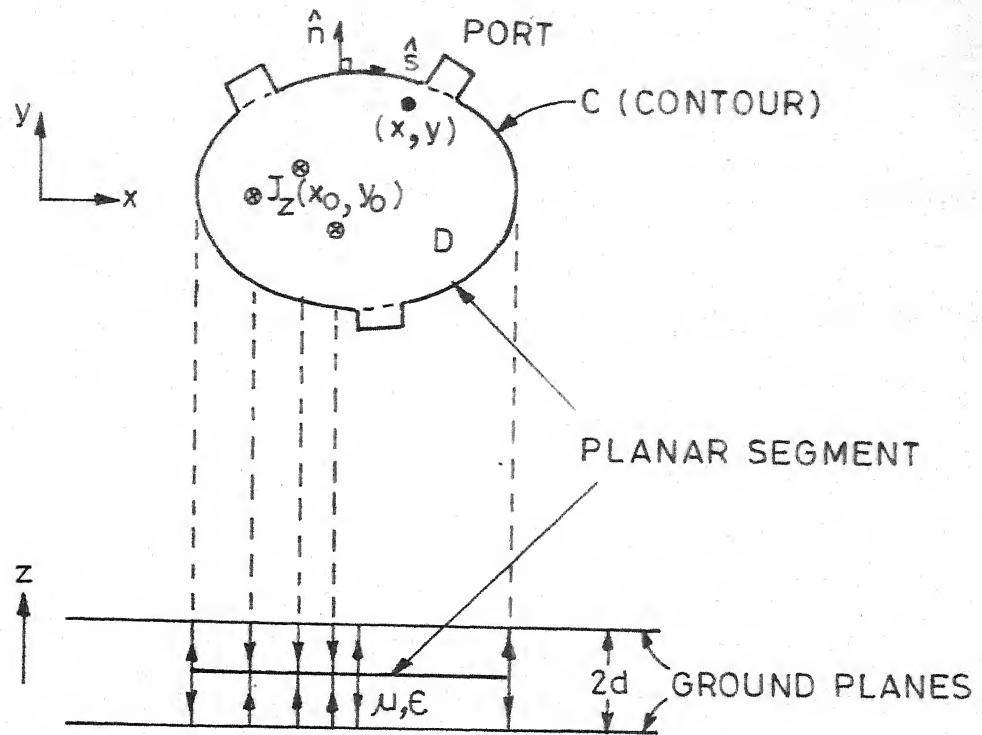


Fig.2.3 Current sources $J_z(x_0, y_0)$ and field point (x, y)

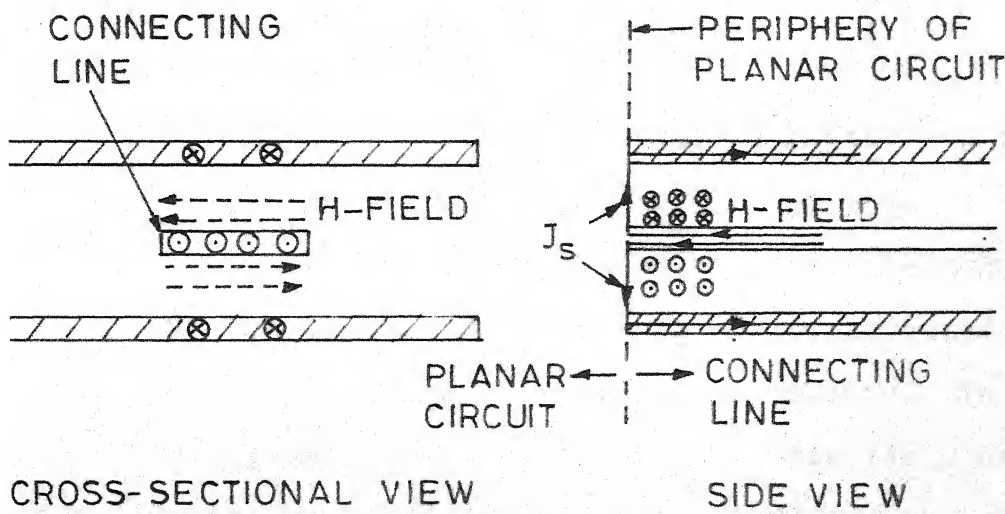


Fig.2.4 Representation of H_{tan} by an equivalent current density J_s

as follows. When the stripline is connected to a coupling port, there will be certain amount of current in the central strip which flows into the planar component. One half of this current flows in the opposite direction in each of the two ground planes. At the boundary where the strip is connected to the planar component, it may be considered that the current loops close by equivalent currents along the z-direction. Figure 2.4 shows the representation of tangential magnetic field (shown as ---) at the interface between planar circuit and the connecting line by an equivalent current density J_s (shown as —) in z-direction. These equivalent currents may be evaluated as given below. At the periphery, the magnetic field can be written from (2.6) and (2.12) as

$$\underline{H} = \frac{1}{j\omega\mu d} \left(\frac{\partial V}{\partial n} \hat{\underline{s}} - \frac{\partial V}{\partial s} \hat{\underline{n}} \right) \quad (2.17)$$

This must be equal to the magnetic field on the other side of the interface between the planar segment and the feeding line. If the magnetic wall condition is imposed all along the periphery, the tangential component of magnetic field at the periphery is modelled to be zero. In the present model, there is a change in magnetic field at the periphery (where coupling ports are located) and the equivalent fictitious surface current J_s in the z-direction, obtained from the boundary condition (2.7), may be written as

$$\underline{J}_s = -\frac{1}{j\omega \mu d} \frac{\partial V}{\partial n} \hat{a}_z \text{ amps/m} \quad (2.18)$$

\underline{J}_s is in the negative z-direction in the region below the conducting patch as shown in Fig. 2.4. The planar component may now be considered to be excited by line currents along z-direction at the coupling ports and $\partial V/\partial n = 0$ can be imposed all along the periphery.

B. Green's functions and impedance matrix

The Green's function $G(\underline{r}/\underline{r}_0)$ for (2.16) is obtained by applying a unit line current source $\delta(\underline{r}-\underline{r}_0)$ flowing along z-direction in the region below the central patch and located at $\underline{r} = \underline{r}_0$. The Green's function $G(\underline{r}/\underline{r}_0)$ is a solution of

$$(\nabla_T^2 + k^2) G(\underline{r}/\underline{r}_0) = -j\omega \mu d \delta(\underline{r}-\underline{r}_0) \quad (2.19)$$

with the boundary condition at the periphery given by

$$\frac{\partial G}{\partial n} = 0 \quad (2.20)$$

Above equations (2.19) and (2.20) yield the Green's functions for both stripline type and microstrip type 2-d components. Now, the voltage at any point on the planar component can be written as

$$V(x, y) = \iint_D G(x, y/x_0, y_0) J_z(x_0, y_0) dx_0 dy_0 \quad (2.21)$$

where $J_z(x_0, y_0)$ denotes a source current density (real or fictitious) injected normally and D denotes the region of the planar component enclosed by magnetic walls.

When the source current is fed only at ports on the periphery, the voltage V at the periphery can be written in terms of line current J_s in z-direction (given by (2.18)) as

$$V(s) = - \int_C G(s/s_0) J_s(s_0) ds_0 \quad (2.22)$$

where s and s_0 are the distances measured along the periphery and the integral is over the entire periphery. Since the line current $J_s(s_0)$ is present only at the coupling ports, equation (2.22) may be written as

$$V(s) = - \sum_j \int_{W_j} G(s/s_0) J_s(s_0) ds_0 \quad (2.23)$$

where W_j indicates the width of the j th coupling port and the summation on the right-hand side is over all the coupling ports. From (2.15) and (2.18), the current i_j fed in at the j th port can be written in terms of the equivalent line current in the z-direction as

$$i_j = -2 \int_{W_j} J_s(s_0) ds_0 \quad (2.24)$$

If the widths of the coupling ports are assumed to be small so that the line current density J_s is distributed uniformly over the width of the port, using (2.24) one obtains

$$J_s(s_0) \text{ for } j\text{th port} = - \frac{i_j}{2W_j} \quad (2.25)$$

Substituting (2.25) in (2.23), $V(s)$ is obtained as

$$V(s) = \sum_j \frac{i_j}{2W_j} \int_{W_j} G(s/s_0) ds_0 \quad (2.26)$$

Above equation gives voltage at any point on the periphery. To obtain the voltage V_i at the i th coupling port, average voltage over the width of the port is taken, i.e.

$$\begin{aligned} V_i &= \frac{1}{W_i} \int_{W_i} V(s) ds \\ &= \sum_j \frac{i_j}{2W_i W_j} \int_{W_i} \int_{W_j} G(s/s_0) ds_0 ds \end{aligned} \quad (2.27)$$

From above equation, the elements of the impedance matrix of the planar component can be written as

$$Z_{ij} = \frac{1}{2W_i W_j} \int_{W_i} \int_{W_j} G(s/s_0) ds_0 ds \quad (2.28)$$

The impedance matrix of a 2-dimensional component is thus determined using the Green's function.

2.2 GREEN'S FUNCTIONS FOR MIXED BOUNDARY PLANAR SEGMENTS

This section describes the development of Green's functions for mixed boundary rectangular and right-angled isosceles triangular segments.

For a given shape of 2-d component with open-boundary (magnetic walls), derivation of the Green's function requires solution of (2.19) with the boundary condition (2.20). But, in case of electric walls the boundary condition

$$G = 0 \quad (2.29)$$

should be satisfied. Thus, the Green's function for a mixed boundary planar segment is derived as solution of (2.19) with boundary condition (2.29) on the electric walls and (2.20) on the remaining sides. Product of delta functions $\delta(x-x_o) \delta(y-y_o)$ contained in the right-hand side of (2.19) represents a line current flowing along z-direction and located at (x_o, y_o) . Such sources have been called as line sources in this section.

The method of images has been employed to derive the Green's functions.

2.2.1 Method of images [17]

An analytical solution of the differential equation (2.19) is obtained by making the right-hand side a periodic function. For this purpose, additional line sources of the type $\delta(x-x_s) \cdot \delta(y-y_s)$ are placed at points (x_s, y_s) outside the region of the planar component. These additional line sources can be thought of as obtained by taking multiple images of the line source at (x_o, y_o) with respect to the various walls of the planar component. The sign of an image source depends on the type of wall across which the image is being taken. The sign of the image source is same for an image across a magnetic wall and is reversed for an image across an electric wall. The source term in (2.19) gets modified and the boundary conditions are satisfied by the voltage V produced by the source and its images. The

image sources should be all outside the region of the planar component so that the solution for G still represents the Green's function for the geometrical shape of the 2-d component. This method cannot be applied to cases where any of the multiple images fall within the region of the planar component itself.

With these additional image sources, the source pattern used in (2.19) becomes periodic and can be expanded in Fourier series. The Green's function can be expressed as an infinite series summation of the functions obtained in the Fourier series expansion. These are the eigenfunctions of (2.13) for the given boundary conditions. The coefficients in the series summation for Green's function can then be obtained by substituting these series expansions in (2.19).

2.2.2 Green's functions for mixed boundary rectangular segments

The Green's function for the rectangle with open boundary as shown in Fig. 2.5(a) is given as [2]

$$G(x, y/x_0, y_0) =$$

$$\frac{i\omega n}{ab} \sum_{m=-\infty}^{\infty} \sum_{n=-\infty}^{\infty} \frac{\cos(k_x x_0) \cos(k_y y_0) \cos(k_x x) \cos(k_y y)}{(k_x^2 + k_y^2 - k^2)} \quad (2.30)$$

$$\text{where } k_x = \frac{m\pi}{a} \text{ and } k_y = \frac{n\pi}{b} .$$

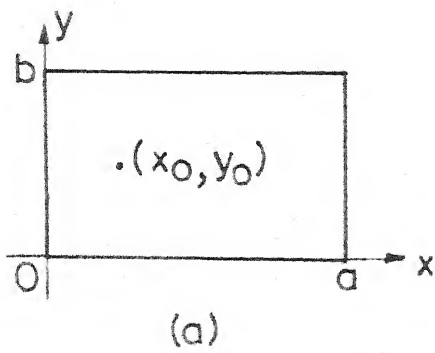
The Green's function for a rectangle with one side as an electric wall and the other three sides being magnetic walls as shown in Fig. 2.5(b) is derived for odd mode analysis of a rectangle having symmetry about an axis parallel to and midway between two of its sides [18]. It is given as

$$G(x, y/x_0, y_0) = \frac{i\omega u d}{ab} \sum_{m=-\infty}^{\infty} \sum_{\substack{n=-\infty \\ \text{odd } n}}^{\infty} \frac{\cos(k_x x_0) \sin(k_y y_0) \cos(k_x x) \sin(k_y y)}{(k_x^2 + k_y^2 - k^2)}$$
(2.31)

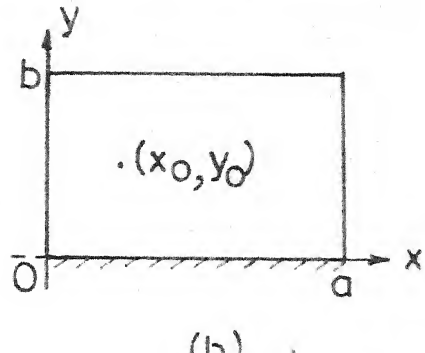
where $k_x = \frac{m\pi}{a}$, $k_y = \frac{n\pi}{2b}$.

Green's function for rectangle with two adjacent electric walls

For the rectangular segment with two adjacent electric walls as shown in Fig. 2.6(a) the Green's function can be obtained by solving equation (2.19) with the boundary condition (2.29) on the electric walls OA and OB and (2.20) on the magnetic walls AC and BC. The additional image sources are obtained by taking multiple images of the line source at (x_0, y_0) with respect to all the four sides of rectangle. The locations of these multiple images are shown in Fig. 2.6(b). From the figure it can be seen that the periodicity of the pattern is $4a$ along the x-direction and $4b$ along the y-direction. So ABCDEFGH is considered as a basic cell which contains 16 line sources in 16 rectangular

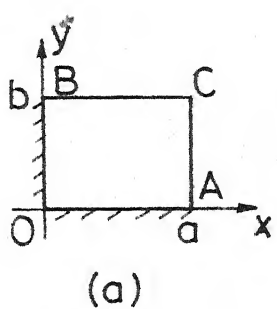


(a)

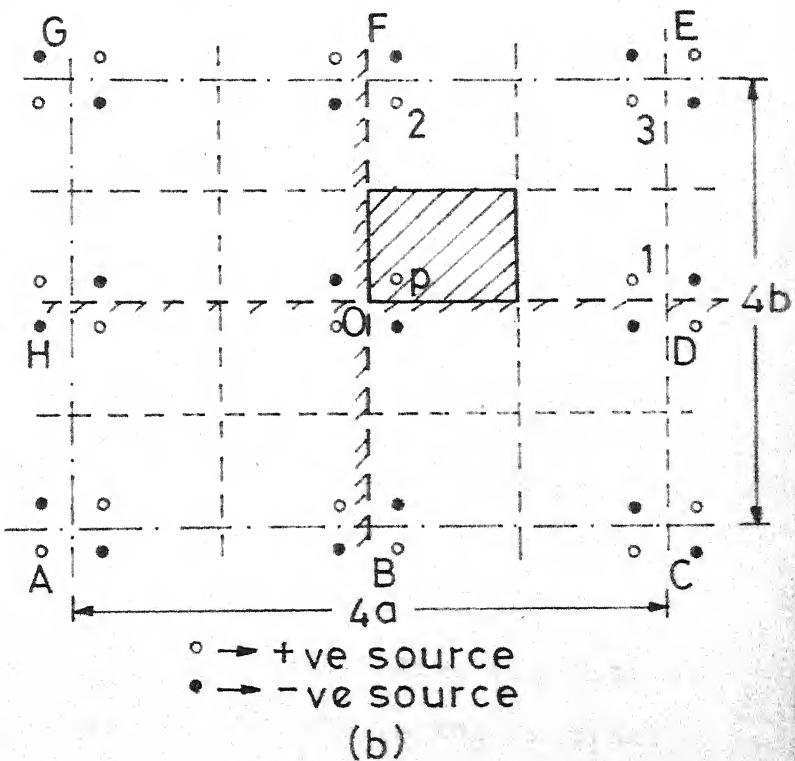


(b)

Fig. 2.5 (a) Rectangular segment with open-boundary
 (b) Rectangular segment with one side as an electric wall



(a)



(b)

Fig. 2.6 (a) Rectangular segment with two adjacent sides as electric walls
 (b) location of image sources

regions as shown in figure. It may be noted that a solution for G with this set of multiple sources will satisfy equation (2.19) in the original region of interest.

For the line source (x_o, y_o) at P shown in Fig. 2.6(b), the coordinates of the image sources in ODEF, can be expressed in terms of (x_o, y_o) as

$$\left. \begin{array}{l} x_1 = 2a - x_o \\ y_1 = y_o \\ \\ x_2 = x_o \\ y_2 = 2b - y_o \\ \\ x_3 = 2a - x_o \\ y_3 = 2b - y_o \end{array} \right\} \begin{array}{l} \text{for image 1} \\ \\ \text{for image 2} \\ \\ \text{for image 3} \end{array}$$

The coordinates for the other images can be obtained from the above ones.

The Fourier series expressions for these 16 line sources which repeat periodically in the two-dimensional spaces are obtained. The corresponding terms of these expressions are added together and the resulting expression, identical to the right-hand side of (2.19) in the original rectangular region, can be expressed as

$$- \frac{j\omega ud}{ab} \sum_{m=1}^{\infty} \sum_{n=1}^{\infty} \sin(k_x x_0) \sin(k_y y_0) \sin(k_x x) \sin(k_y y) \quad (2.32)$$

odd(m,n)

$$\text{where } k_x = \frac{m\pi}{2a} \quad \text{and} \quad k_y = \frac{n\pi}{2b} \quad .$$

It can be verified that the functions $\sin(k_x x) \sin(k_y y)$ in (2.32) satisfy the boundary conditions (2.28) and (2.29) for the rectangle shown in Fig. 2.6(a). The functions $\sin(k_x x) \sin(k_y y)$ are the eigenfunctions for this rectangle. The Green's function G can be written in terms of these eigenfunctions as

$$G(x, y/x_0, y_0) = \sum_{m=1}^{\infty} \sum_{n=1}^{\infty} A_{mn} \sin(k_x x) \sin(k_y y) \quad (2.33)$$

odd(m,n)

Substituting (2.33) in the right-hand side of (2.19), one obtains

$$(\nabla_T^2 + k^2)G = \sum_{m=1}^{\infty} \sum_{n=1}^{\infty} A_{mn} (k^2 - k_x^2 - k_y^2) \sin(k_x x) \sin(k_y y) \quad (2.34)$$

odd(m,n)

Since (2.32) and (2.34) are equal for all values of x and y , the values of A_{mn} are obtained by comparison as

$$A_{mn} = \frac{j\omega ud}{ab} \frac{\sin(k_x x_0) \sin(k_y y_0)}{(k_x^2 + k_y^2 - k^2)} \quad (2.35)$$

Substituting (2.35) in (2.33), one gets

$$G(x, y/x_0, y_0) = \frac{j\omega ud}{ab} \sum_{m=1}^{\infty} \sum_{n=1}^{\infty} \frac{\sin(k_x x_0) \sin(k_y y_0) \sin(k_x x) \sin(k_y y)}{(k_x^2 + k_y^2 - k^2)} \quad (2.36)$$

odd(m,n)

which is the required Green's function for (2.19) for the rectangle with two adjacent electric walls shown in Fig. 2.6(a).

Green's function for rectangle with two parallel electric walls

For the rectangular segment with two parallel electric walls as shown in Fig. 2.7(a), the boundary condition (2.29) is valid on the sides OA and BC and on the other sides (2.20) is satisfied. In this case, the periodicity of the pattern is $2a$ along the x -direction and $2b$ along the y -direction. The locations of additional line sources are shown in Fig. 2.7(b). The basic cell which repeats itself is ABCD. By carrying out steps similar to that in the earlier case, the Green's function is found to be

$$G(x, y/x_0, y_0)$$

$$= \frac{jwud}{ab} \sum_{m=-\infty}^{\infty} \sum_{n=-\infty}^{\infty} \frac{\cos(k_x x_0) \sin(k_y y_0) \cos(k_x x) \sin(k_y y)}{(k_x^2 + k_y^2 - k^2)} \quad (2.37)$$

$$\text{where } k_x = \frac{m\pi}{a} \quad \text{and} \quad k_y = \frac{n\pi}{b} \quad .$$

Green's function for rectangle with three electric walls

For the rectangular segment with three electric walls as shown in Fig. 2.8(a), the boundary condition (2.20) is valid on the side BC and on the other three sides (2.29) is satisfied. The positions of additional images are shown in Fig. 2.8(b). The periodicity of the pattern is $2a$ along

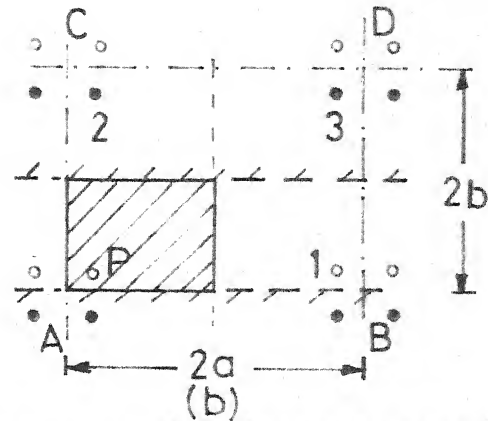
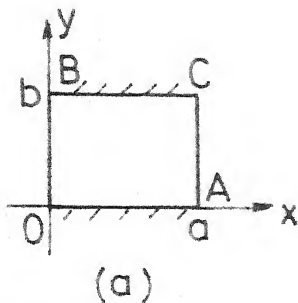


Fig. 2.7 (a) Rectangular segment with two parallel sides as electric walls
 (b) location of image sources

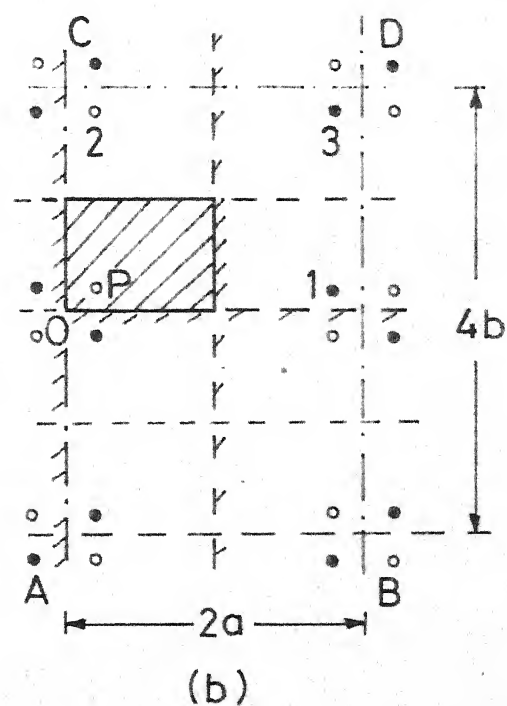
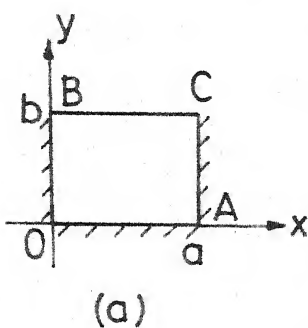


Fig. 2.8 (a) Rectangular segment with three sides as electric walls
 (b) location of image sources

the x-axis and 4b along the y-axis. The basic cell which repeats itself is ABCD. By carrying out similar steps as in the earlier cases, the Green's function is found to be

$$G(x, y/x_0, y_0)$$

$$= \frac{j\omega\mu d}{ab} \sum_{\substack{m=-\infty \\ \text{Odd}}}^{\infty} \sum_{n=-\infty}^{\infty} \frac{\sin(k_x x_0) \sin(k_y y_0) \sin(k_x x) \sin(k_y y)}{(k_x^2 + k_y^2 - k^2)} \quad (2.38)$$

$$\text{where } k_x = \frac{m\pi}{a} \text{ and } k_y = \frac{n\pi}{2b} .$$

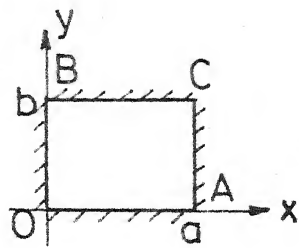
Green's function for rectangle with electric wall boundary

For the rectangular segment with electric wall boundary as shown in Fig. 2.9(a), the boundary condition (2.29) is valid for all the sides. The positions of additional line sources are shown in Fig. 2.9(b). The basic cell is ABCD. In this case, the periodicity of the pattern is 2a along the x-axis and 2b along the y-axis. By carrying out similar steps, the Green's function is found to be

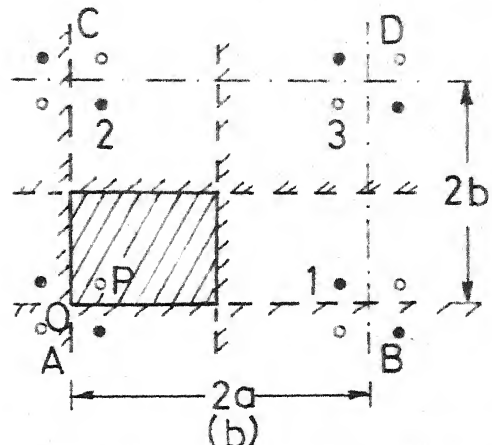
$$G(x, y/x_0, y_0)$$

$$= \frac{j\omega\mu d}{ab} \sum_{\substack{m=-\infty \\ \text{Odd}}}^{\infty} \sum_{n=-\infty}^{\infty} \frac{\sin(k_x x_0) \sin(k_y y_0) \sin(k_x x) \sin(k_y y)}{(k_x^2 + k_y^2 - k^2)} \quad (2.39)$$

$$\text{with } k_x = \frac{m\pi}{a} \text{ and } k_y = \frac{n\pi}{b} .$$



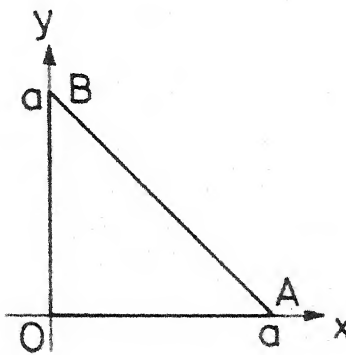
(a)



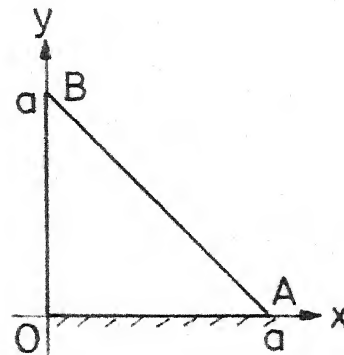
(b)

g. 2.9 (a) Rectangular segment with electric wall boundary

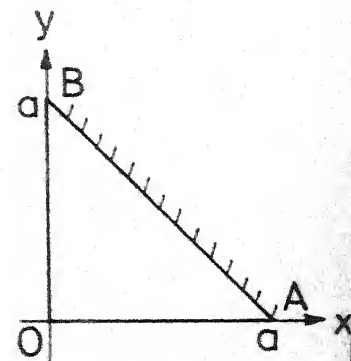
(b) location of image sources



(a)



(b)



(c)

g. 2.10 (a) An isosceles right-angled triangle with open-boundary

(b) with one side as electric wall

(c) with hypotenuse as electric wall

2.2.3 Green's functions for mixed boundary isosceles right-angled triangular segments

The Green's function for an isosceles right-angled triangle with open boundary as shown in Fig. 2.10(a) is given as [5]

$$G(x, y/x_0, y_0)$$

$$= \sum_{m=-\infty}^{\infty} \sum_{n=-\infty}^{\infty} \frac{j \omega \mu d T(x_0, y_0) T(x, y)}{2[(m^2+n^2) \pi^2 - a_k^2]^2} \quad (2.40)$$

$$\text{where } T(x, y) = \cos \frac{m\pi x}{a} \cos \frac{n\pi y}{a} + (-1)^{m+n} \cos \frac{n\pi x}{a} \cos \frac{m\pi y}{a} \quad (2.41)$$

The Green's function for an isosceles right-angled triangle (shown in Fig. 2.10(b)) with OA as an electric wall and the others two sides being magnetic walls is given as [5]

$$G(x, y/x_0, y_0)$$

$$= 2j \omega \mu d \sum_{\substack{m=-\infty \\ \text{odd}(m,n)}}^{\infty} \sum_{n=-\infty}^{\infty} \frac{U(x_0, y_0) U(x, y)}{[(m^2+n^2)\pi^2 - 4a_k^2]^2} \quad (2.42)$$

$$\text{where } U(x, y) = \cos \frac{m\pi x}{2a} \sin \frac{n\pi y}{2a} - (-1)^{(m+n/2)} \cos \frac{n\pi x}{2a} \sin \frac{m\pi y}{2a} \quad (2.43)$$

The Green's function when hypotenuse is an electric wall as shown in Fig. 2.10(c) is given as [5]

$$G(x, y/x_o, y_o)$$

$$= \sum_{m=-\infty}^{\infty} \sum_{n=-\infty}^{\infty} \frac{j \omega \mu d W(x_o, y_o) W(x, y)}{2[(m^2 + n^2) \pi^2 - a^2 k^2]} \quad (2.44)$$

where

$$W(x, y) = \cos \frac{m\pi x}{a} \cos \frac{n\pi y}{a} - (-1)^{m+n} \cos \frac{n\pi x}{a} \cos \frac{m\pi y}{a} \quad (2.45)$$

Green's function when Hypotenuse and one of the other sides are electric walls

As in the earlier rectangular cases, the right-hand side of (2.19) can be made periodic by placing additional line sources outside the right-angled triangle shown in Fig. 2.11(a). The boundary condition (2.20) is valid on side OA and on the other two sides, (2.29) is satisfied. The positions of additional line sources are obtained by taking multiple images of the original line source at (x_o, y_o) with respect to various walls of the triangle. The periodicity of the pattern is $4a$ along both the x and y directions. The basic cell which repeats itself is ABCD which contains 32 line sources as shown in Fig. 2.11(b).

For the line source (x_o, y_o) at P in Fig. 2.11(b), the coordinates of the image line sources can be expressed in terms of (x_o, y_o) as

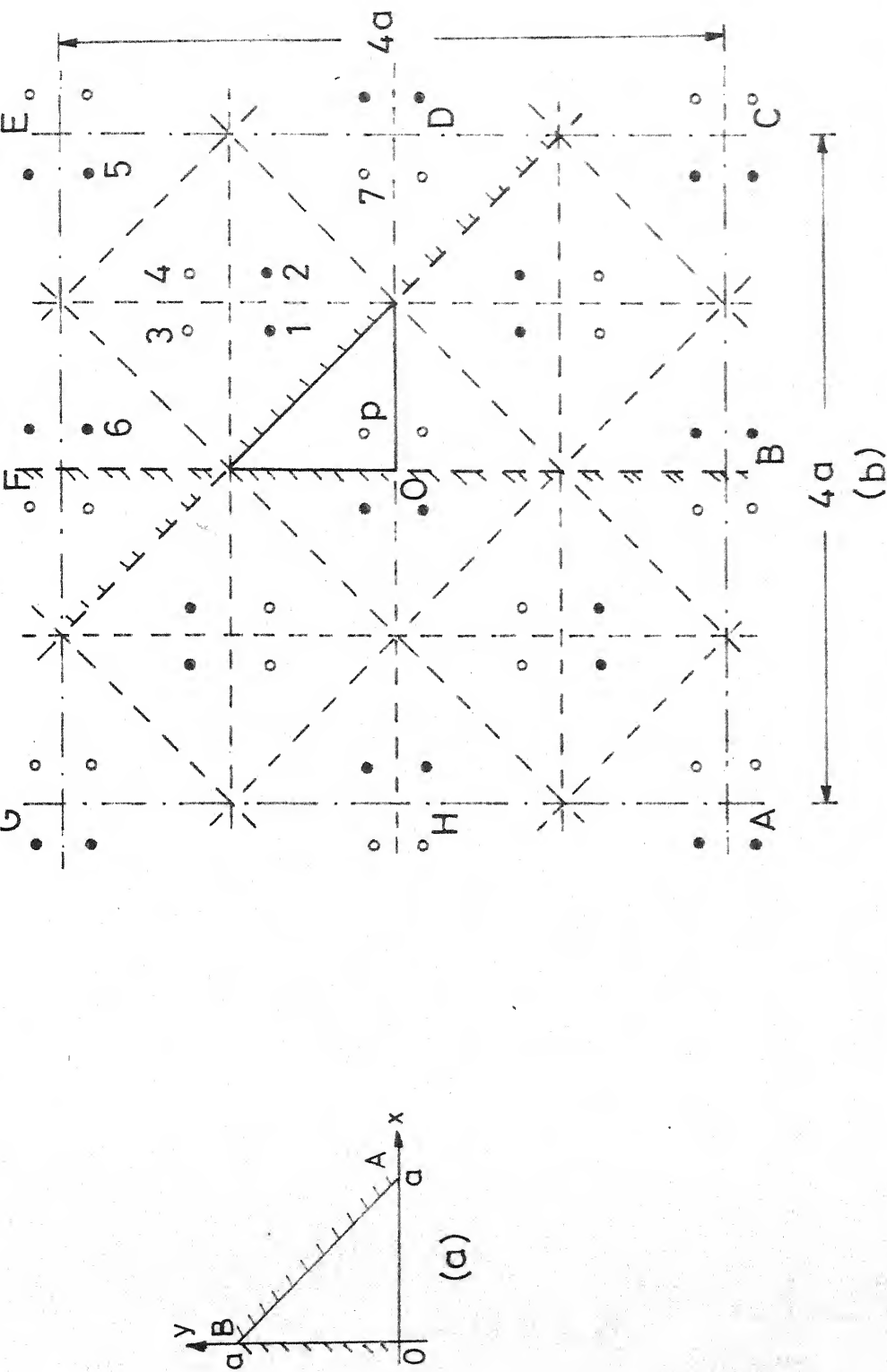


Fig. 2.11(a) An isosceles right-angled triangle with hypotenuse and one of the other sides as electric walls
 (b) location of image sources

$$\begin{array}{ll}
 x_1 = a - y_o & x_4 = a + y_o \\
 y_1 = a - x_o & y_4 = a + x_o \\
 x_2 = a + y_o & x_5 = 2a - x_o \\
 y_2 = a - x_o & y_5 = 2a - y_o \\
 x_3 = a - y_o & x_6 = x_o \\
 y_3 = a + x_o & y_6 = 2a - y_o \\
 & x_7 = 2a - x_o \\
 & y_7 = y_o
 \end{array}$$

Adding the corresponding terms in Fourier series expressions for each of the line sources in the basic cell, the resulting expression equivalent to the right-hand side of (2.19) can be expressed as

$$-\frac{j\omega\mu d}{a^2} \sum_{m=-\infty}^{\infty} \sum_{n=-\infty}^{\infty} \sin k_x x \cos k_y y P(x_o, y_o) \quad (2.46)$$

odd unequal
(m, n)

where

$$k_x = \frac{m\pi}{2a} \quad \text{and} \quad k_y = \frac{n\pi}{2a} \quad (2.47)$$

$$\text{and } P(x, y) = \sin k_x x \cos k_y y + (-1)^{\frac{m+n}{2}} \sin k_y x \cos k_x y \quad (2.48)$$

It can be verified that

$$\begin{aligned}
 & \sum_{m=-\infty}^{\infty} \sum_{n=-\infty}^{\infty} \sin(k_x x) \cos(k_y y) P(x_o, y_o) \\
 &= \sum_{m=-\infty}^{\infty} \sum_{n=-\infty}^{\infty} (-1)^{\frac{m+n}{2}} \sin(k_y x) \cos(k_x y) P(x_o, y_o) \quad (2.49)
 \end{aligned}$$

Using (2.49), expression (2.46) can be rewritten as

$$-\frac{j\omega\mu d}{2a^2} \sum_{-\infty}^{\infty} \sum_{-\infty}^{\infty} P(x_0, y_0) P(x, y) \quad (2.50)$$

The function $P(x, y)$ satisfies the boundary condition (2.20) on hypotenuse and (2.29) on the other sides for the triangle shown in Fig. 2.11(a). So, G can be expressed as

$$G = \sum_{-\infty}^{\infty} \sum_{-\infty}^{\infty} A_{mn} P(x, y) \quad (2.51)$$

Substituting (2.51) in the left-hand side of (2.19) one obtains

$$(\nabla_T^2 + k^2)G = \sum_{-\infty}^{\infty} \sum_{-\infty}^{\infty} [k^2 - \frac{\pi^2}{4a^2} (m^2 + n^2)] A_{mn} P(x, y) \quad (2.52)$$

By comparing (2.50) and (2.52) one obtains A_{mn} as

$$A_{mn} = \frac{2j\omega\mu d P(x_0, y_0)}{(m^2 + n^2)\pi^2 - 4a^2 k^2} \quad (2.53)$$

Substituting (2.53) in (2.51), one gets

$$G(x, y/x_0, y_0) = 2j\omega\mu d \sum_{\substack{-\infty \\ \text{odd, unequal}}}^{\infty} \sum_{\substack{-\infty \\ (m, n)}}^{\infty} \frac{P(x_0, y_0) P(x, y)}{(m^2 + n^2)\pi^2 - 4a^2 k^2} \quad (2.54)$$

which is the Green's function for (2.19) for the triangular segment shown in Fig. 2.11(a).

Green's function when Hypotenuse is magnetic wall and the other two sides are electric walls

For the triangular segment shown in Fig. 2.12(a), the

boundary condition (2.29) is valid on the sides OA and OB and on the other side (2.20) is satisfied. In this case, the periodicity of the pattern is $2a$ along both the x and y directions. The positions of additional line sources are shown in Fig. 2.12(b). The basic cell which repeats itself is ABCD. By carrying out steps similar to that in the previous case, the Green's function is found to be

$$G(x, y/x_0, y_0) = j \omega \mu d \sum_{m=-\infty}^{\infty} \sum_{n=-\infty}^{\infty} \frac{Q(x_0, y_0) Q(x, y)}{2[(m^2+n^2)\pi^2 - a^2 k^2]} \quad (2.55)$$

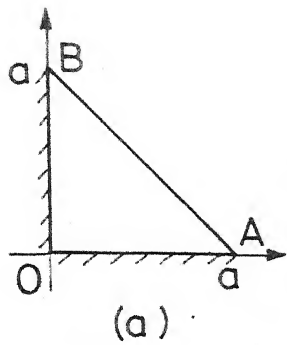
where

$$Q(x, y) = \sin \frac{m\pi x}{a} \sin \frac{n\pi y}{a} + (-1)^{m+n} \sin \frac{n\pi x}{a} \sin \frac{m\pi y}{a} \quad (2.56)$$

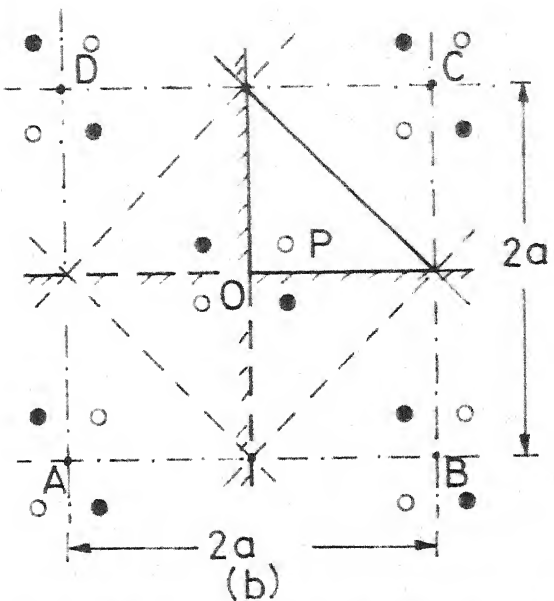
Green's function when all the sides are electric walls

For the triangular segment shown in Figs. 2.13(a), the boundary condition (2.29) is valid on all the sides. The periodicity of the pattern is $2a$ along both the x and y directions. The locations of additional image sources are shown in Fig. 2.13(b). ABCD is considered as a basic cell which contains 8 line sources in 8 triangular regions. By carrying out similar steps as in the earlier cases, the Green's function is found to be

$$G(x, y/x_0, y_0) = j \omega \mu d \sum_{m=-\infty}^{\infty} \sum_{n=-\infty}^{\infty} \frac{S(x_0, y_0) S(x, y)}{2[(m^2+n^2)\pi^2 - a^2 k^2]} \quad (2.57)$$

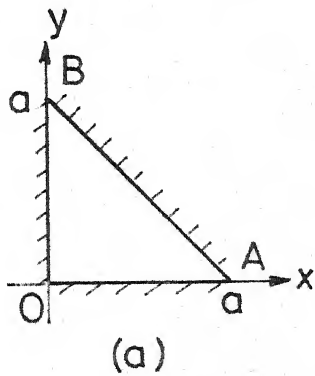


(a)

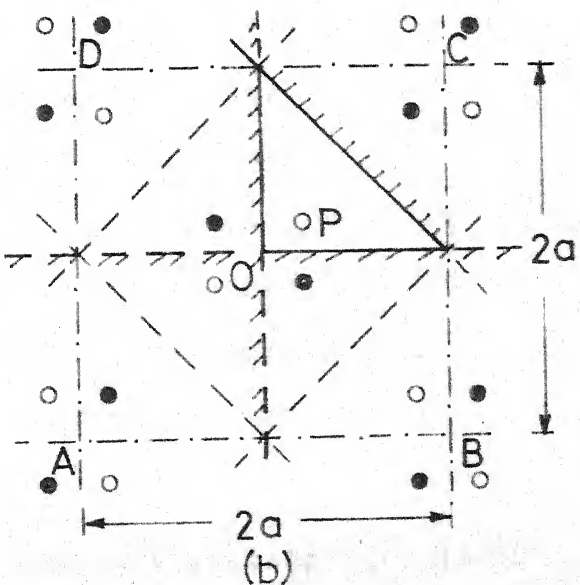


(b)

g. 2.12(a) An isosceles right-angled triangle with hypotenuse as magnetic wall and other two sides as electric walls
 (b) location of image sources



(a)



(b)

g. 2.13(a) An isosceles right-angled triangle with electric wall boundary
 (b) location of image sources

where

$$S(x, y) = \sin \frac{m\pi x}{a} \sin \frac{n\pi y}{a} - (-1)^{m+n} \sin \frac{n\pi x}{a} \sin \frac{m\pi y}{a} \quad (2.58)$$

2.3 DISCUSSION

The method of images used in this chapter is restricted to the shapes enclosed by boundaries which are straight lines. This is because the only mirror surface which gives a point image for a point source is a plane mirror. Only for a few polygonal shapes, the images can be uniquely specified without any of the image sources falling within the region of the planar segment. If all sides of the polygon are magnetic walls or all sides are electric walls, the internal angle at each vertex should be a submultiple of 180° . For polygons with mixed boundary conditions, the angles at all vertices where one side is electric wall and the other magnetic wall should be 90° or a submultiple of 90° . Other vertices should have angles which are submultiples of 180° . Thus, the method of images can be used for only rectangular and triangular shapes.

Green's functions of mixed boundary planar segments derived in this chapter are used for analyzing mixed boundary rectangular microstrip antennas in next chapter.

Chapter Three

MIXED BOUNDARY RECTANGULAR MICROSTRIP ANTENNAS

This chapter gives details of the investigations carried out on mixed boundary rectangular microstrip antennas. In the first section, the method of analysis used is described. Later sections describe the theoretical analysis and experimental results of various mixed boundary rectangular microstrip antennas. For comparison purpose, an open-boundary rectangular microstrip antenna [11] - [13] is also studied. The last section gives details about measurement of mutual coupling between one-side shorted rectangular microstrip antennas.

All antennas are fabricated on copper cladded 0.318 cm thick polysterene substrate whose relative permittivity is 2.55 and are fed by coaxial feed-lines.

3.1 METHOD OF ANALYSIS

Green's function approach and segmentation method are used for finding the input impedance and voltage around the periphery of the antennas. Radiation field components are calculated by using the voltage around the periphery.

3.1.1 Green's function approach

The microstrip antenna under consideration is analyzed in terms of an equivalent network model. The procedure is

illustrated in Fig. 3.1. The physical boundary of the antenna is extended outward to account for the fringing field around the edges [11], [19], and a magnetic wall is considered to exist at this boundary. This magnetic wall boundary is divided into several sections and each section is considered as a port. The number of ports along any edge is decided such that the widths of these ports are small enough to have negligible field variation over the portwidths. The feed-location is optimized for an input impedance of 50 ohms, so that there is no necessity to use any external impedance matching network for measurements. For this, various possible locations of the feed-points are considered as external ports. The widths of those ports are taken equal to the diameter of coaxial feed-line. The impedance matrix of such a multiport network model is calculated from (2.28) using the corresponding Green's function. The elements of this impedance matrix are purely reactive and the poles of the input reactance yield the resonance frequencies of the planar structure (the losses in the structure and the radiated power having been ignored).

The losses due to radiation effect of the antenna are accounted for by loading the ports of the ideal multiport network model (excluding feed-ports) by radiation conductances [11],[20] as illustrated in Fig. 3.1. The values

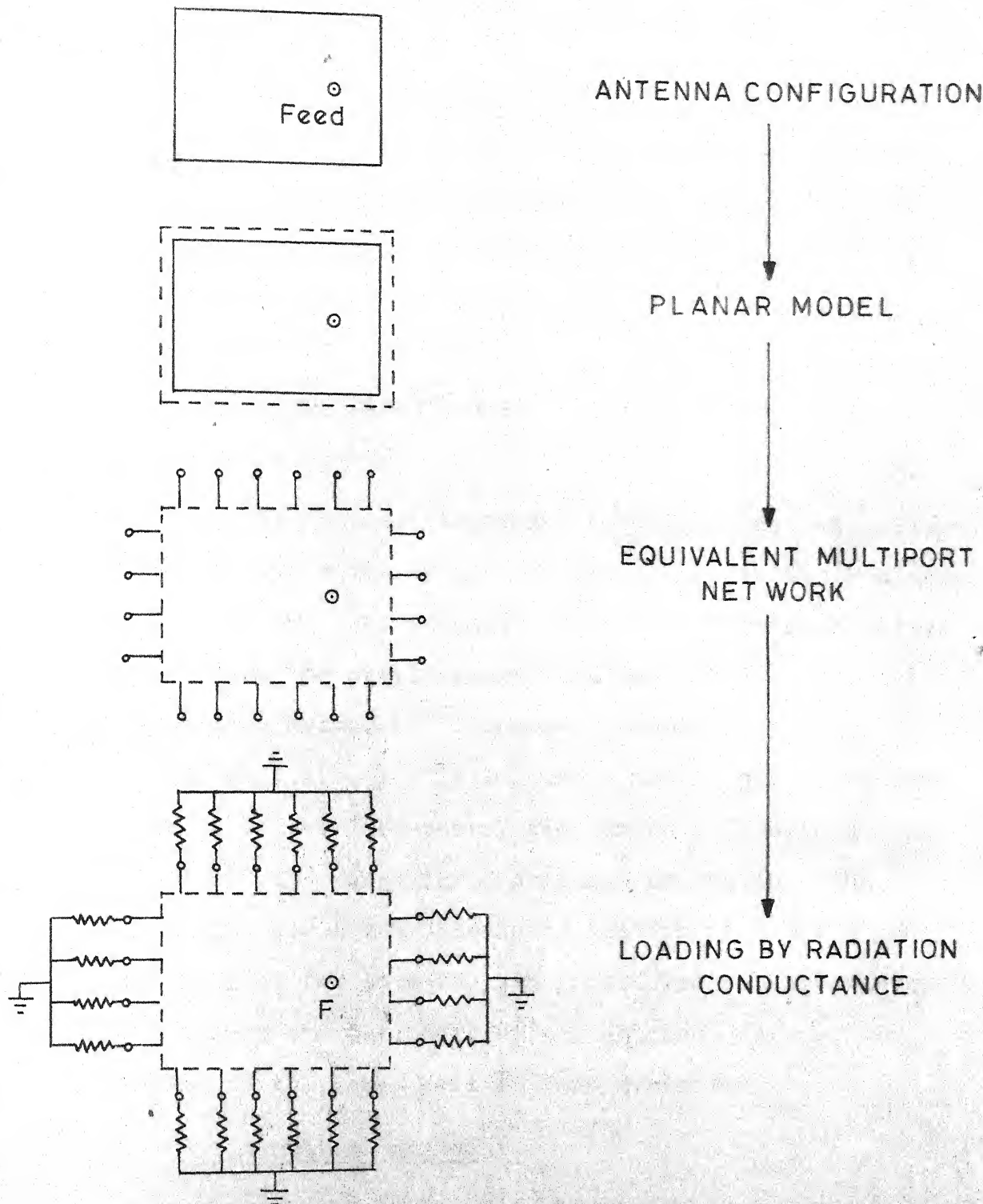


Fig.3.1 Procedure to analyze microstrip antennas by Green's function approach

of the radiation conductances which terminate the ports are calculated as follows : (i) calculate the radiation conductance for each of the four sides of the planar model, (ii) distribute the radiation conductance to each of the ports, the values being proportional to the respective portwidths, (iii) the conductances thus calculated are considered to be connected at the mid-points of the respective ports.

The impedance matrix of the loaded equivalent multiport network is evaluated by considering the radiation conductance multiport network as one network and the multiport network representing the planar element as another network, using segmentation method [2] discussed in Section 3.1.2. The diagonal elements of this impedance matrix give the input impedances at the feed-ports, from which a feed-location, where input impedance is 50 ohms can be chosen. The element Z_{ij} gives the voltage at the i th port for a unit input current fed into the j th port. The voltage distribution around the periphery of the antenna, for any arbitrary location of the input port is thus evaluated.

3.1.2 Segmentation method

Consider an example of loaded equivalent network model of rectangular antenna shown in Fig. 3.1. The multiport network representing the planar element is considered as one segment (α) and radiation conductance multiport network (β)

as another segment as shown in Fig. 3.2. The entries in the Z-matrix of β -segment are all zeros except the diagonal elements which are equal to radiation resistance values. The Z-matrix of the loaded network is obtained from the Z-matrices of the individual segments using segmentation method, as follows :

The Z-matrices of individual components can be written together as

$$\begin{bmatrix} \underline{V}_p \\ \underline{V}_c \\ \underline{V}_d \end{bmatrix} = \begin{bmatrix} \underline{Z}_{pp} & \underline{Z}_{pc} & \underline{Z}_{pd} \\ \underline{Z}_{cp} & \underline{Z}_{cc} & \underline{Z}_{cd} \\ \underline{Z}_{dp} & \underline{Z}_{dc} & \underline{Z}_{dd} \end{bmatrix} \begin{bmatrix} \underline{i}_p \\ \underline{i}_c \\ \underline{i}_d \end{bmatrix} \quad (3.1)$$

where, subscript p denotes external ports and subscripts c and d represent connected ports (c_1 and d_1 are connected together, c_2 and d_2 are connected together and so on). The interconnection constraints can be expressed as

$$\underline{V}_c = \underline{V}_d, \quad (3.2a)$$

and

$$\underline{i}_c + \underline{i}_d = 0 \quad (3.2b)$$

Substituting (3.2) in (3.1) and eliminating \underline{V}_p , \underline{V}_c and \underline{i}_d , one gets

$$\underline{i}_c = (\underline{Z}_{cc} - \underline{Z}_{cd} - \underline{Z}_{dc} + \underline{Z}_{dd})^{-1} (\underline{Z}_{dp} - \underline{Z}_{cp}) \underline{i}_p \quad (3.3)$$

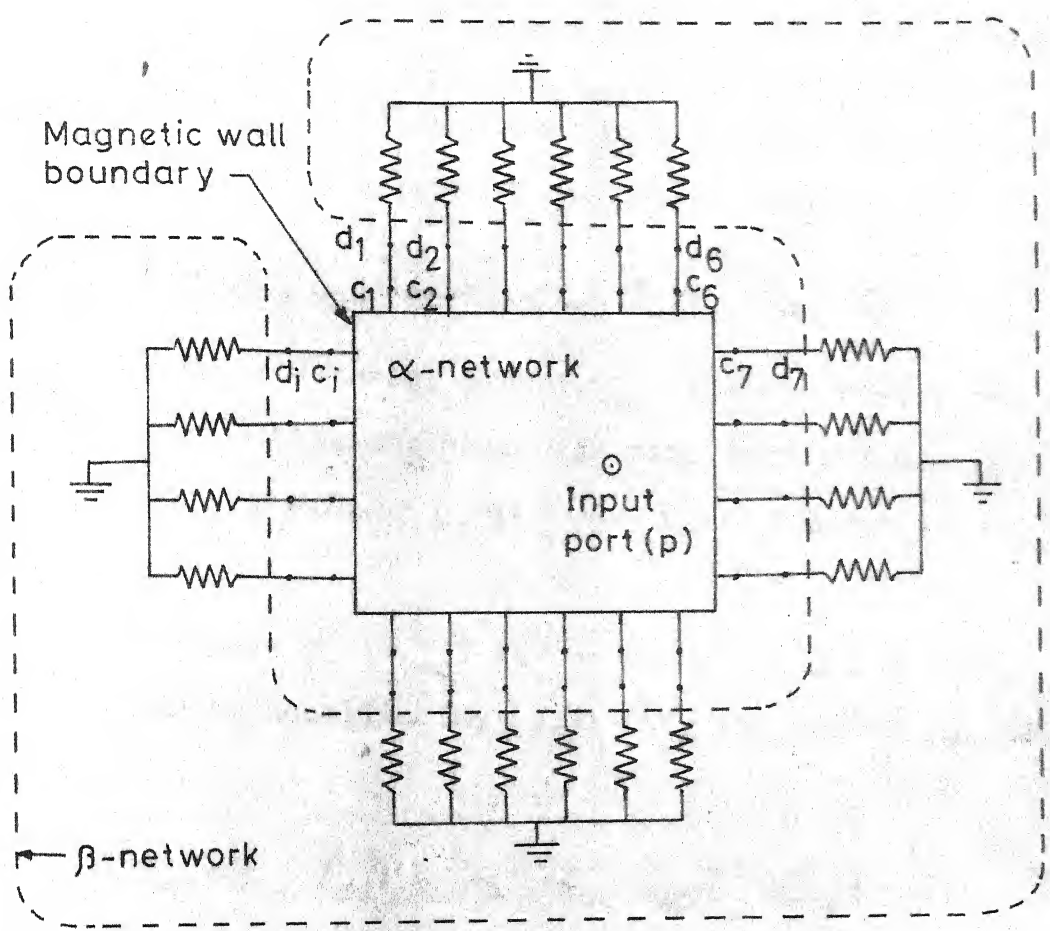


Fig.3-2 Segmentation for analyzing the loaded multiport network model of Fig.3-1

Substituting (3.3) into the first equation of (3.1) and using $\underline{i}_c = -\underline{i}_d$, the Z-matrix of the overall network is obtained as

$$\underline{Z}_p = \underline{Z}_{pp} + (\underline{Z}_{pc} - \underline{Z}_{pd})(\underline{Z}_{cc} - \underline{Z}_{cd} - \underline{Z}_{dc} + \underline{Z}_{dd})^{-1} (\underline{Z}_{dp} - \underline{Z}_{cp}) \quad (3.4)$$

For a single external p-port, \underline{Z}_p directly yields the input impedance of the antenna. For more than one p-port, the diagonal elements of \underline{Z}_p give the input impedances at p-ports.

Voltages \underline{V}_c ($= \underline{V}_d$) at the connected ports can be obtained by substituting (3.3) into the second equation of (3.1) as

$$\underline{V}_c = [\underline{Z}_{cp} + (\underline{Z}_{cc} - \underline{Z}_{cd})(\underline{Z}_{cc} - \underline{Z}_{cd} - \underline{Z}_{dc} + \underline{Z}_{dd})^{-1} (\underline{Z}_{dp} - \underline{Z}_{cp})] \underline{i}_p \quad (3.5)$$

3.1.3 Radiation pattern calculations

The radiation pattern of the antenna is calculated from the voltage distribution along the periphery as described below.

The voltage at any port along the periphery, given by (3.5) can be expressed as equivalent Huygen's magnetic current source [13]

$$\bar{K}' = -2 (\hat{n} \times \hat{z}) E_z \quad (3.6)$$

where \bar{K}' is the surface magnetic current density, E_z is the electric field at the respective port location directed along z -axis, \hat{n} is the outward unit vector normal to the magnetic wall and \hat{z} is the unit vector along z -axis. The relative orientation of \bar{K}' , \hat{n} and E_z are shown in Fig. 3.3(a). The factor of 2 in (3.6) takes care of the image of the magnetic current with respect to the ground plane. In the case of planar microstrip antennas, it is assumed that there is no field variation along the z -axis since the thickness of the dielectric substrate is very small, so (3.6) can be expressed as

$$\bar{K} = 2(\hat{n} \times \hat{z}) V_z, \quad (3.7)$$

where \bar{K} represents the equivalent magnetic line current source which is obtained by integrating (3.6) over the thickness of the substrate and V_z is the voltage at the corresponding port location. The electric vector potential for the magnetic current given by (3.7) can be expressed as [13]

$$\bar{F}(\bar{r}) = \epsilon_0 \int_c \frac{\bar{K}(\bar{r}')}{4\pi |\bar{r}-\bar{r}'|} e^{-jk_0 |\bar{r}-\bar{r}'|} d\bar{l}(\bar{r}') \quad (3.8)$$

where k_0 is the free-space propagation constant and \bar{r} and \bar{r}' are the distance vectors of the field point and source point respectively as shown in Fig. 3.3(b). The integration is

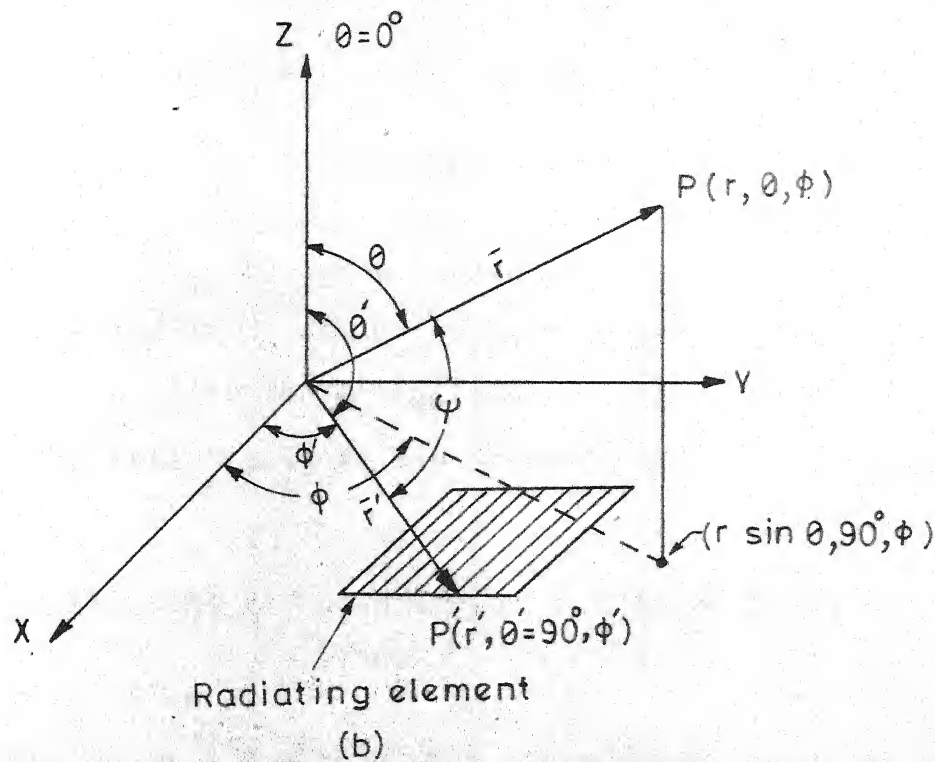
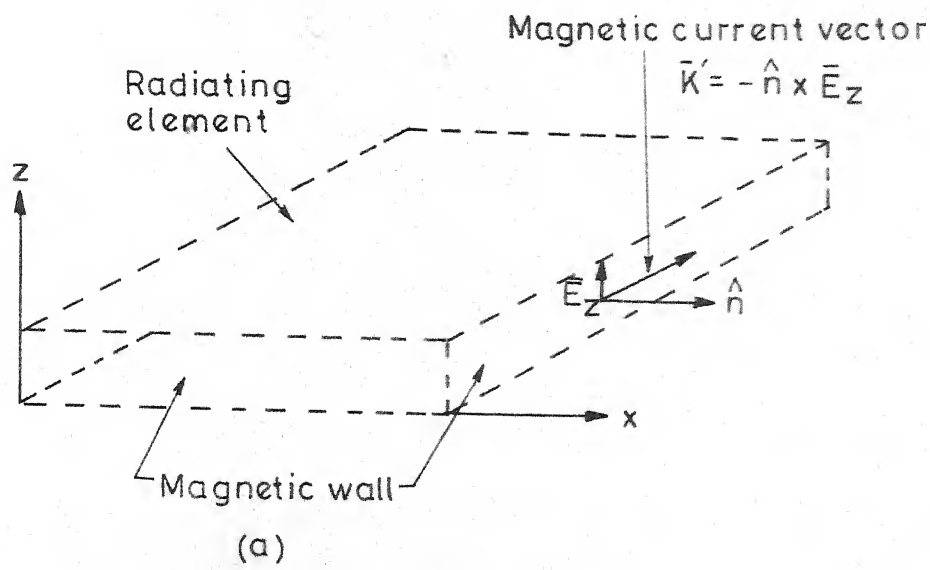


Fig.3.3(a) Orientation of electric field and magnetic current vectors

(b) Co-ordinate system

performed along the periphery of the antenna. As the voltage over a portwidth is considered to be constant, (3.8) reduces to

$$\bar{F}(\bar{r}) = \frac{\epsilon_0}{4\pi} \sum_{i=1}^m \bar{K}_i(\bar{r}') \int \frac{1}{c_i |\bar{r}-\bar{r}'|} e^{-jk_0 |\bar{r}-\bar{r}'|} dl(\bar{r}') \quad (3.9)$$

where m is the number of ports considered along the periphery. The integration is thus performed over each portwidth and summed up to evaluate the vector potential. The far-fields at a distance \bar{r} from the origin are given by

$$\bar{E}_\theta = \eta \bar{H}_\varphi = jk_0 \bar{F}_\varphi = -jk_0 (\bar{F}_x \sin\varphi - \bar{F}_y \cos\varphi) \quad (3.10a)$$

$$\bar{E}_\varphi = -\eta \bar{H}_\theta = -jk_0 \bar{F}_\theta = -jk_0 (\bar{F}_x \cos\theta \cos\varphi + \bar{F}_y \cos\theta \sin\varphi) \quad (3.10b)$$

where \bar{F}_x and \bar{F}_y are x and y components of the electric vector potential $\bar{F}(\bar{r})$. \bar{E}_θ and \bar{E}_φ are in space-quadrature, and after calculating their amplitudes and phases from (3.10), the polarization pattern can be evaluated in any direction and plane.

3.2 RECTANGULAR PATCH ANTENNA WITH OPEN-BOUNDARY

3.2.1 Analysis

The Green's function of a rectangular planar segment given in (2.30) is used for analysis and is written as

$$G(x, y/x_0, y_0) = \frac{j\omega\mu d}{ab} \sum_{m=-\infty}^{\infty} \sum_{n=-\infty}^{\infty} \frac{\cos(k_x x_0) \cos(k_y y_0) \cos(k_x x) \cos(k_y y)}{k_x^2 + k_y^2 - k^2} \quad (3.11)$$

where $k_x = \frac{m\pi}{a}$ and $k_y = \frac{n\pi}{b}$.

The resonant frequency for any mode can be obtained from

$$f = \frac{1}{2\pi} \sqrt{\frac{1}{\mu\epsilon} \left[\left(\frac{m\pi}{a}\right)^2 + \left(\frac{n\pi}{b}\right)^2 \right]} \quad (3.12)$$

where a and b are the effective length and width of the rectangle respectively.

A square patch antenna of dimensions, length (L) and width (W) equal to 4.0 cm, excited at (1,0) mode as shown in Fig. 3.4(a) is analyzed. The thickness of the substrate is taken as $h = 0.318$ cm and the relative permittivity ϵ_r is taken as 2.55. The effective length and width are obtained by adding extension due to fringing field at the open-ends to physical dimensions and they are equal to 4.56 cm. Sufficient accuracy in input VSWR with less computation time is obtained by considering seven ports along the non-radiating edges (as the field varies sinusoidally along the length) and two ports along the radiating edges (as the field is almost uniform along the width) as shown in Fig. 3.4(b).

For (1,0) mode there is a sinusoidal variation of the field along the length, so the input impedance changes if feed-point is changed along the length. If a feed-point is considered at the mid-way of width, (0,1) mode is not excited. Hence, several feed-points are considered along the length and at the mid-way of width and the feed-location where input impedance is 50 ohms is

CONFIDENTIAL LIBRARY
Acc. No. A 82690

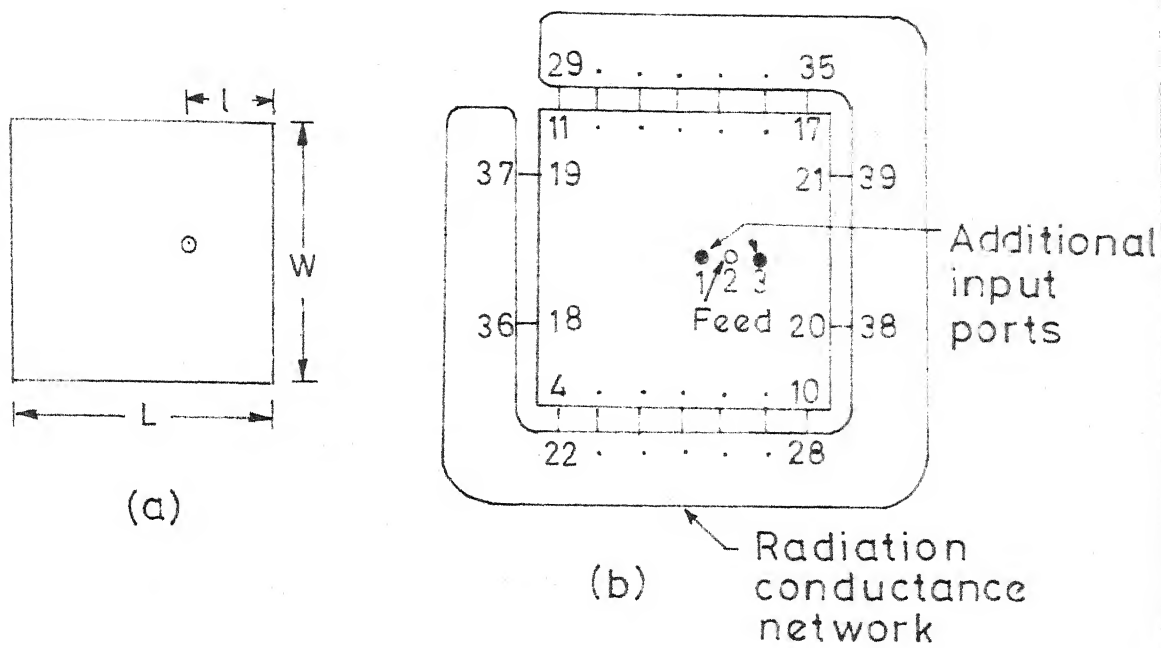


Fig.3.4 (a) Square patch antenna and
(b) its segmented network

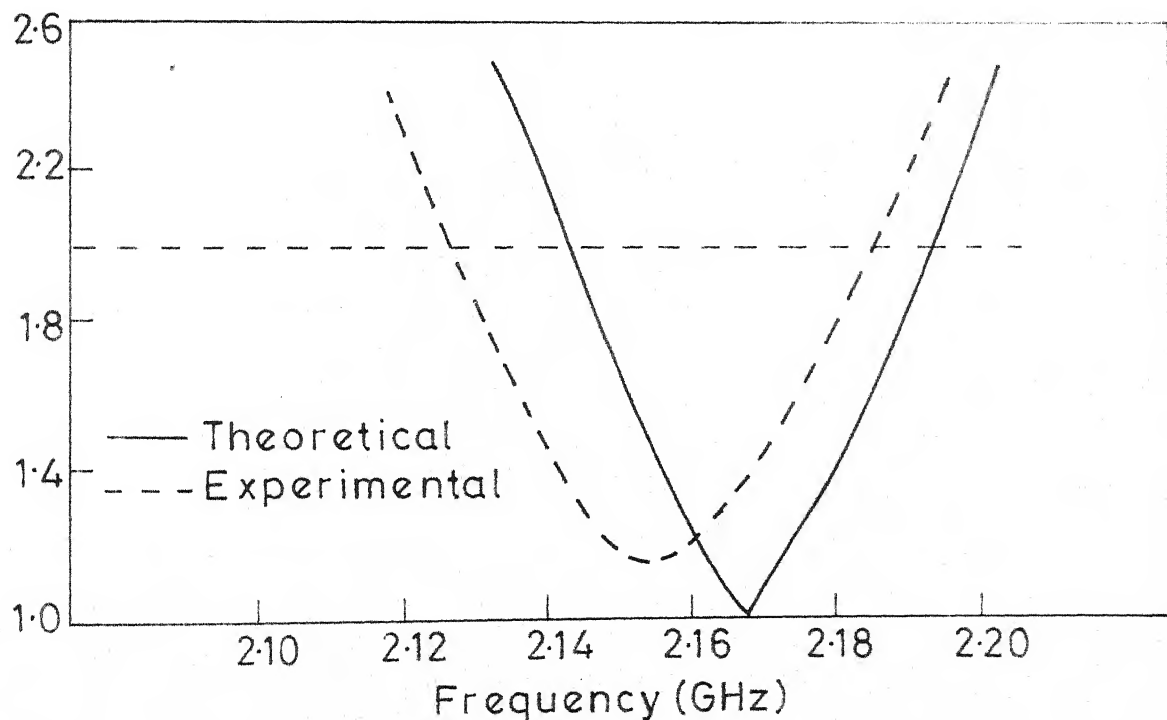


Fig.3.5 Theoretical and experimental variations of input VSWR with frequency

3.2.2 Bandwidth

Depending upon system objectives, the bandwidth of an antenna is limited either by its radiation characteristics or by its input VSWR characteristics. In case of microstrip patch antennas, the resonant behaviour causes the bandwidth to be limited by input VSWR and it may be defined as the frequency range for which VSWR remains less than two.

Theoretical variation of VSWR with frequency is plotted in Fig. 3.5. The bandwidth of the antenna is 52 MHz (2.4 percent, centre frequency $f_o = 2.167 \text{ GHz}$).

The antenna is fabricated on copper cladded 0.318 cm thick polystyrene substrate whose ϵ_r is 2.55 and is fed by coaxial line. The measured bandwidth is 59 MHz (2.7 percent, centre frequency $f_o = 2.155 \text{ GHz}$). Measured bandwidth is greater than the theoretical value because conductor losses, dielectric losses and losses due to surface wave propagation are ignored in the analysis.

3.2.3 Radiation pattern

For a unit current excitation at the feed-point, the voltage distribution along the periphery is obtained from (3.5). Using this voltage distribution, the radiation field components E_θ and E_ϕ are calculated in $\varphi = 0^\circ$ and $\varphi = 90^\circ$ planes at centre frequency. It is noted that only E_θ component is present in $\varphi = 0^\circ$ plane and E_ϕ is present in $\varphi = 90^\circ$

plane and they are plotted in Figs. 3.7(a) and (b) respectively. The 3-db beamwidths in $\varphi = 0^\circ$ and $\varphi = 90^\circ$ planes are 100° and 80° respectively.

Experimental set up for measuring the radiation field components E_θ and E_φ in a plane is shown in Fig. 3.6. For measuring the fields in the orthogonal plane, the antenna is rotated by 90° . Experimental variations of E_θ in $\varphi = 0^\circ$ plane and E_φ in $\varphi = 90^\circ$ plane are also plotted in Figs. 3.7(a) and (b) respectively. The experimental beamwidths in $\varphi = 0^\circ$ and $\varphi = 90^\circ$ planes are 80° and 60° respectively. These experimental beamwidths are smaller than the theoretical values. Experimental values of E_θ are much less than the theoretical values for $\theta > 60^\circ$. This decrease in E_θ is due to i) the excitation of surface waves which causes flow along the substrate surface and ii) the presence of finite ground plane.

3.3 RECTANGULAR PATCH ANTENNA WITH ONE SIDE AS AN ELECTRIC WALL

3.3.1 Analysis

The Green's function of a rectangle with one side as electric wall given in (2.31) is used for analysis and is written as

$$G(x, y/x_0, y_0) = \frac{j\omega\mu d}{ab} \sum_{m=-\infty}^{\infty} \sum_{n=-\infty}^{\infty} \text{odd } m \frac{\cos(k_x x_0) \sin(k_y y_0) \cos(k_x x) \sin(k_y y)}{(k_x^2 + k_y^2 - k^2)} \quad (3.13)$$

where $k_x = \frac{m\pi}{2a}$ and $k_y = \frac{n\pi}{b}$.

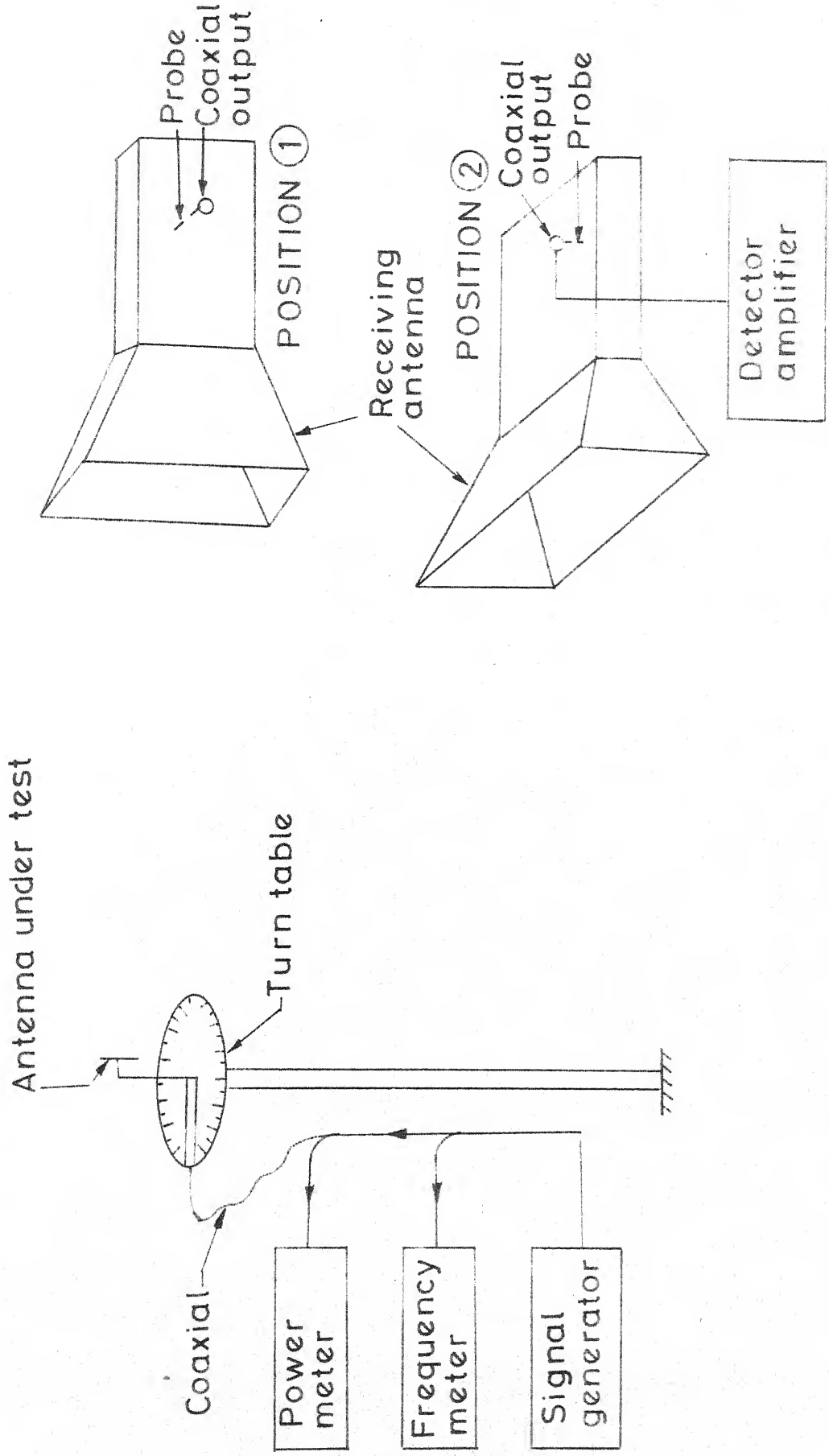


Fig.3.6 Experimental setup for radiation pattern measurement

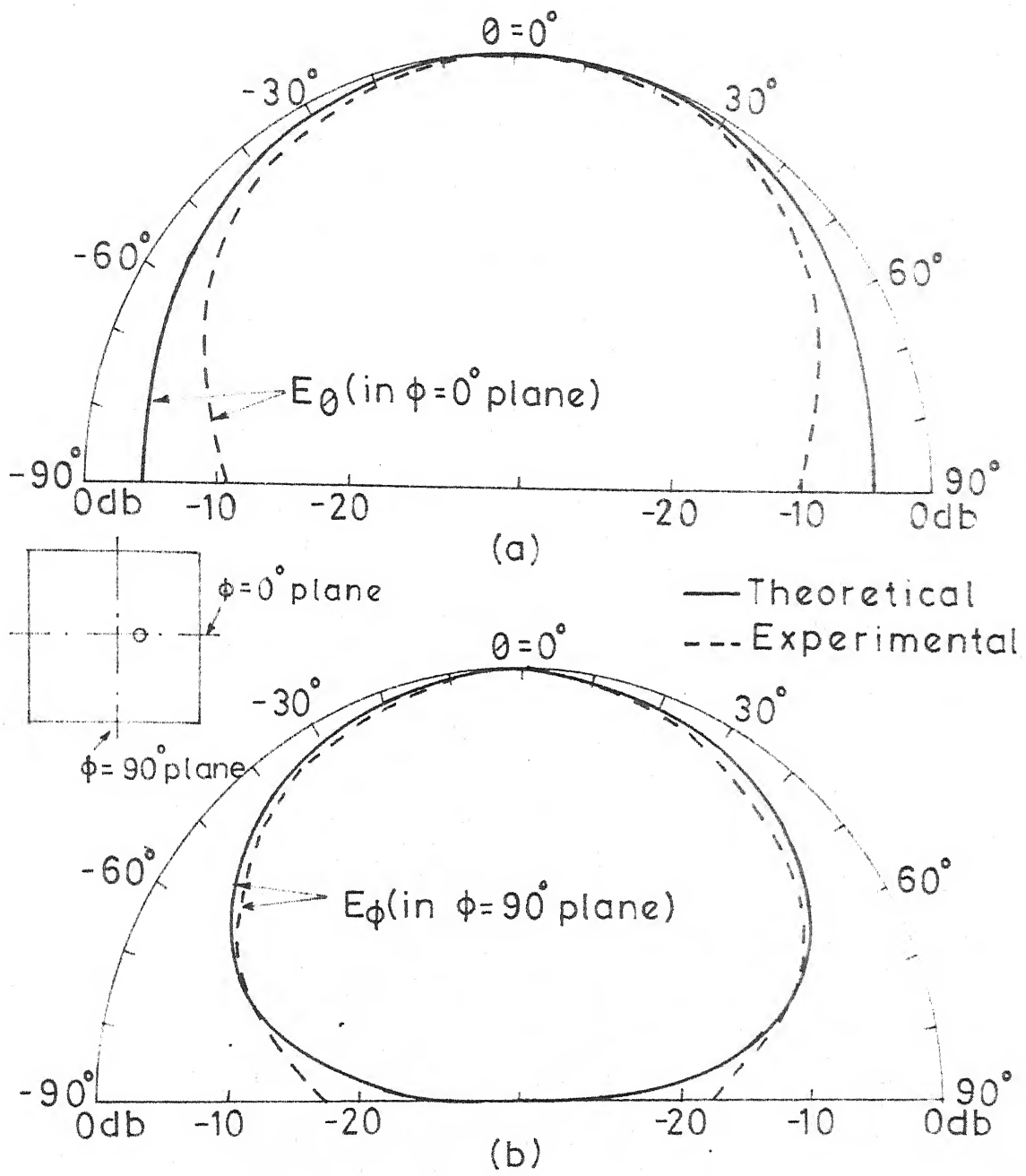


Fig.3.7 Theoretical and experimental radiation patterns (a) E_θ in $\phi=0^\circ$ plane and (b) E_ϕ in $\phi=90^\circ$ plane of a square patch antenna shown in Fig. 3.4(a)

The resonant frequency for any mode can be obtained from

$$f = \frac{1}{2\pi} \sqrt{\frac{1}{\mu\epsilon} \left[\left(\frac{m\pi}{2a}\right)^2 + \left(\frac{n\pi}{b}\right)^2 \right]} \quad (3.14)$$

where a and b are the effective length and width of the rectangle respectively.

A rectangular patch antenna with one side as electric wall of dimensions, length $L = 2.0$ cm and width $W = 4.0$ cm, excited at $(1,0)$ mode as shown in Fig. 3.8(a) is analyzed. There is no fringing field at the shorted edge and hence while finding the effective length, extension is considered only at one side (open-end). Effective length and width are obtained as 2.28 cm and 4.56 cm respectively. No ports are considered along the shorted edges for analysis. For $(1,0)$ mode excitation, feed-location must be along the length and at the mid-way of width as in the previous case. So, several feed-ports are considered near the shorted edge as shown in Fig. 3.8(b) and the feed-location where input impedance is 50 ohms is obtained at $\lambda = 0.39$ cm.

3.3.2 Bandwidth

Theoretical and experimental variations of VSWR with normalised frequency are plotted in Fig. 3.9. The calculated and measured bandwidths of the antenna are 47 MHz (2.17 percent, centre frequency $f_o = 2.162$ GHz) and 45 MHz (2.17 percent, centre frequency $f_o = 2.077$ GHz) respectively.

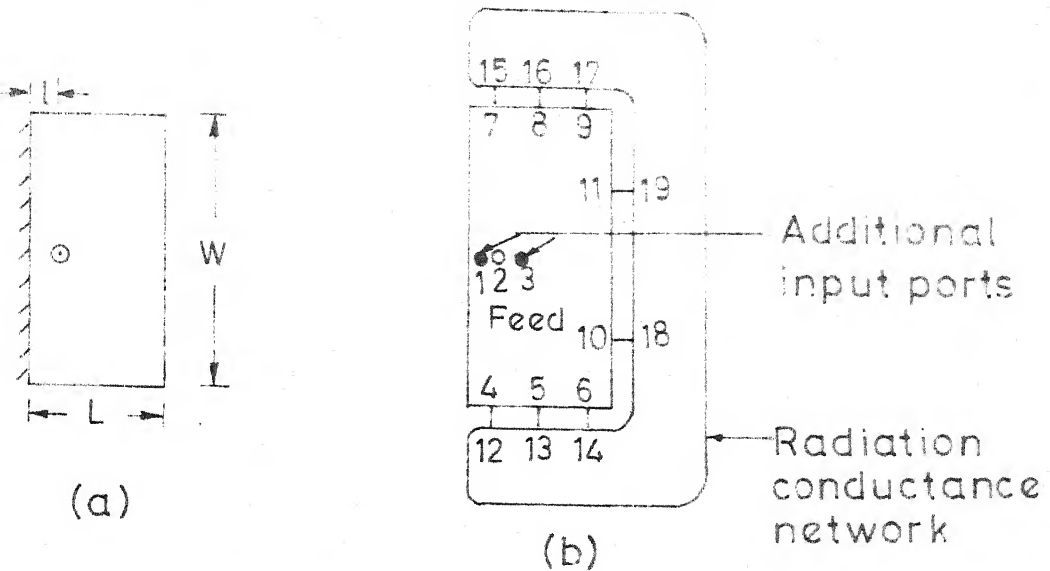


Fig.3.8(a) Rectangular patch antenna with one side as electric wall and
 (b) its segmented network

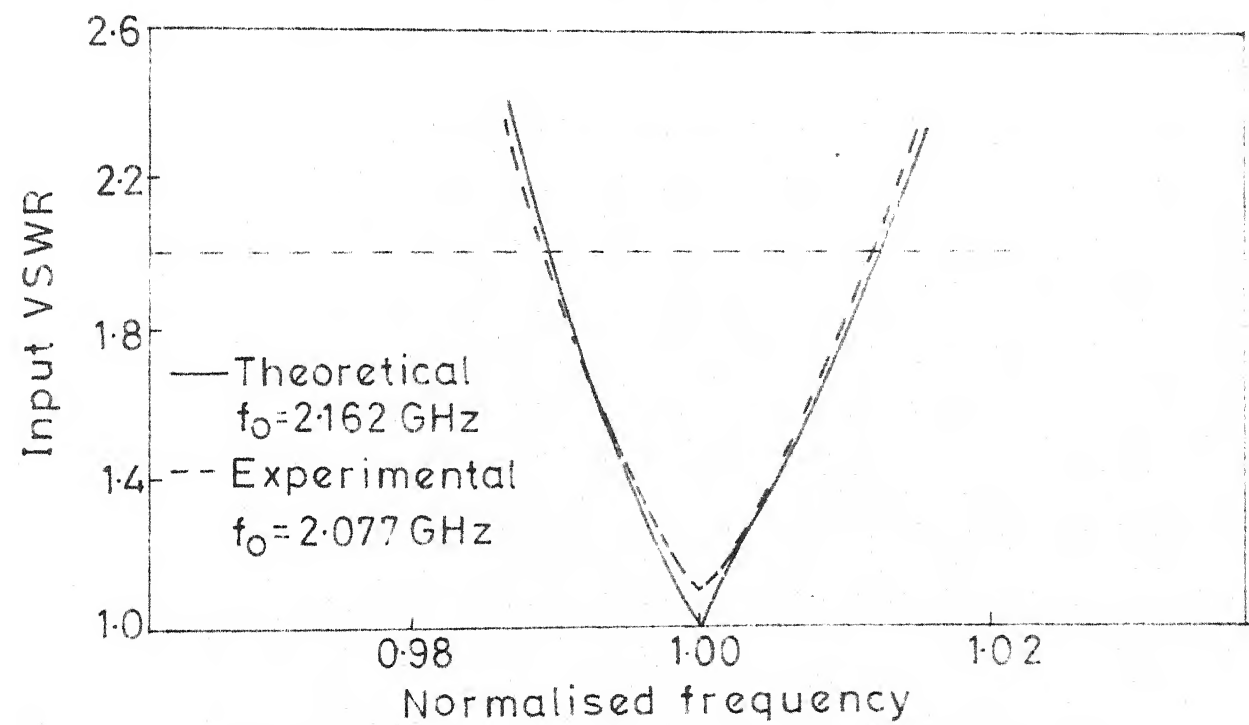


Fig.3.9 Theoretical and experimental variations of input VSWR with normalised frequency

During fabrication of the antenna, electric wall at one side is established by shorting the upper radiator and lower ground plane using wires at various points along the edge. Better results may be obtained by doing effective shorting, using plated through holes.

Since the square patch antenna with open boundary discussed in the previous section also operates at the same centre frequency as this antenna, the comparison of the two can be carried out. It is noted that the bandwidth of the rectangular antenna with one side shorted is around 9 percent less than that of the antenna with open-boundary. Bandwidth is less in one side short-circuited antenna because there is only one radiating edge which makes the radiated power less, compared to open-boundary antenna.

3.3.3 Radiation pattern

Theoretical and experimental variations of radiation field components E_θ (in $\varphi = 0^\circ$ plane) and E_φ (in $\varphi = 90^\circ$ plane) at centre frequency are plotted in Figs. 3.10(a) and (b) respectively. The theoretical 3-db beamwidths in $\varphi = 0^\circ$ and $\varphi = 90^\circ$ planes are 115° and 85° respectively. Corresponding experimental 3-db beamwidths are 98° and 72° respectively. These beamwidths are more than those of the square patch antenna with open boundary. Broader radiation pattern is obtained because of the fact that there is only one radiating edge in this case.

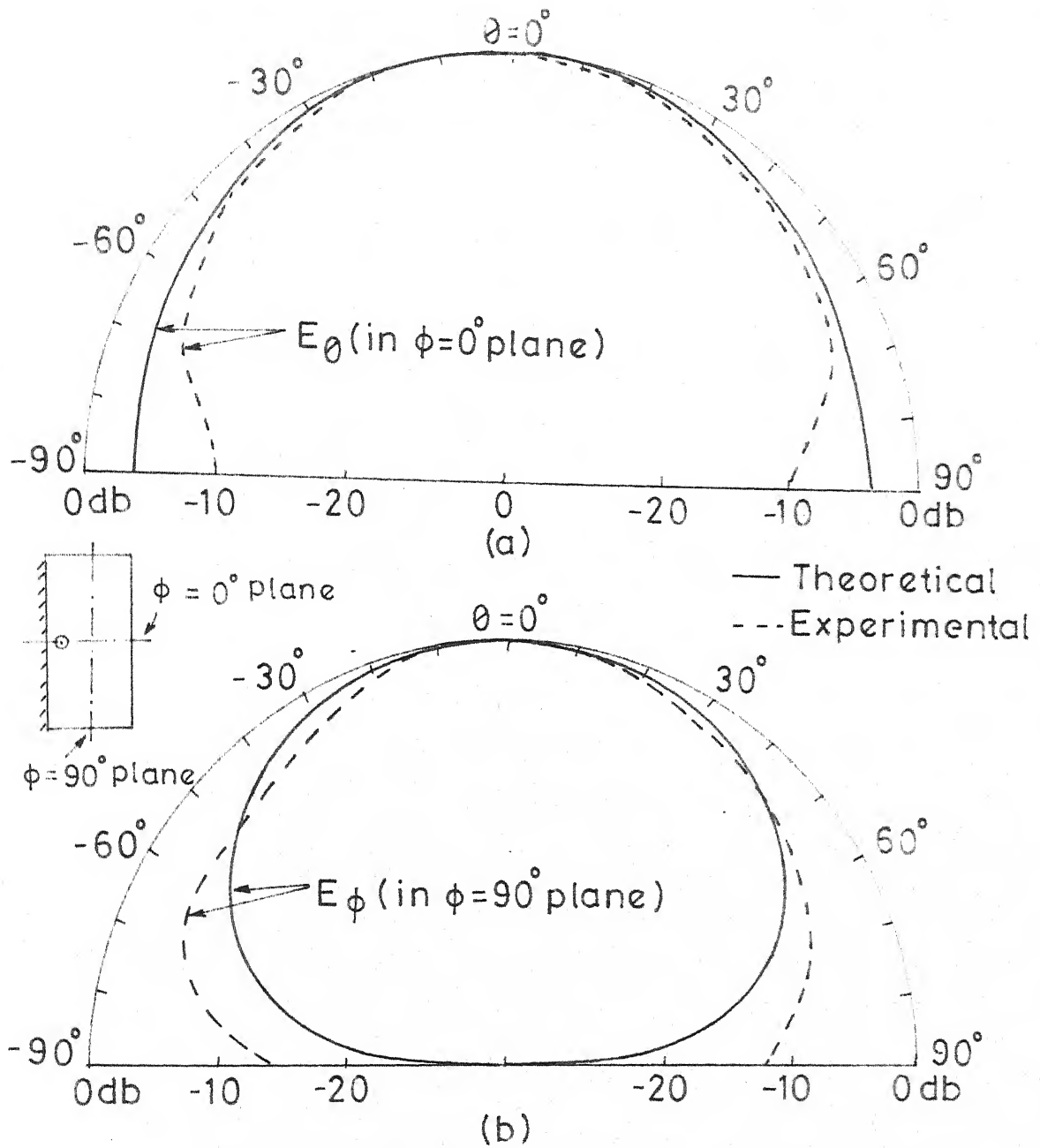


Fig. 3.10 Theoretical and experimental radiation patterns (a) E_θ in $\phi = 0^\circ$ plane (b) E_ϕ in $\phi = 90^\circ$ plane of a rectangular patch antenna with one side as an electric wall shown in Fig. 3.9(a)

3.4 RECTANGULAR PATCH ANTENNA WITH TWO ADJACENT SIDES AS ELECTRIC WALLS

3.4.1 Analysis

The Green's function of a rectangle with two adjacent sides as electric walls given in (2.36) is used for analysis and is written as

$$G(x, y/x_0, y_0) = \frac{j \omega \mu d}{ab} \sum_{\substack{m=-\infty \\ \text{odd}(m,n)}}^{\infty} \sum_{n=-\infty}^{\infty} \frac{\sin(k_y y_0) \sin(k_x x_0) \sin(k_x x) \sin(k_y y)}{k_x^2 + k_y^2 - k^2} \quad (3.15)$$

where $k_x = \frac{m\pi}{2a}$ and $k_y = \frac{n\pi}{2b}$

The resonant frequency for any mode can be obtained from

$$f = \frac{1}{2\pi} \sqrt{\frac{1}{\mu \epsilon} \left[\left(\frac{m\pi}{2a} \right)^2 + \left(\frac{n\pi}{2b} \right)^2 \right]} \quad (3.16)$$

where a and b are the effective length and width of the rectangle respectively.

A square patch antenna with two adjacent sides as electric walls of dimensions, length (L) and width (W) equal to 2.0 cm, excited at (1,1) mode as shown in Fig. 3.11(a) is analyzed. As there is no fringing field at the shorted edges for obtaining the effective length and width, extension is considered only at one side (i.e. open-end) and are equal to 2.28 cm. For analysis, no ports are considered along the shorted edges. For exciting (1,1) mode the feed-location must

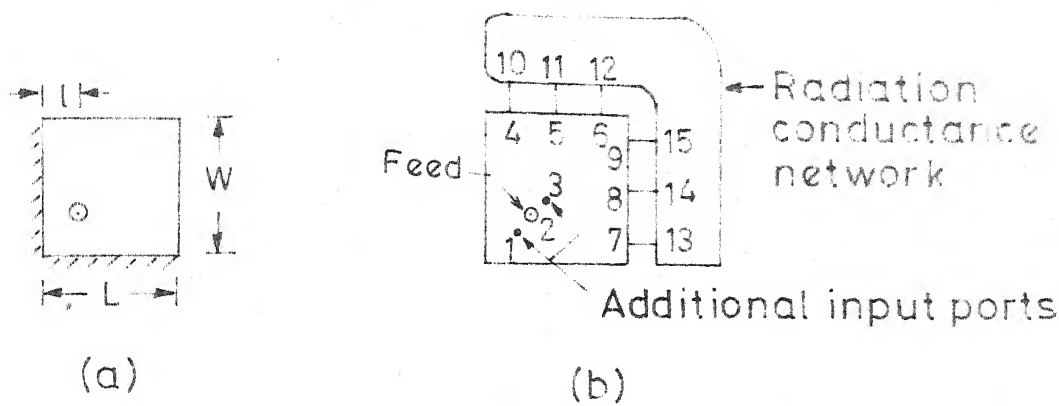


Fig.3.11(a) A square patch antenna with two adjacent sides as electric walls and
 (b) its segmented network

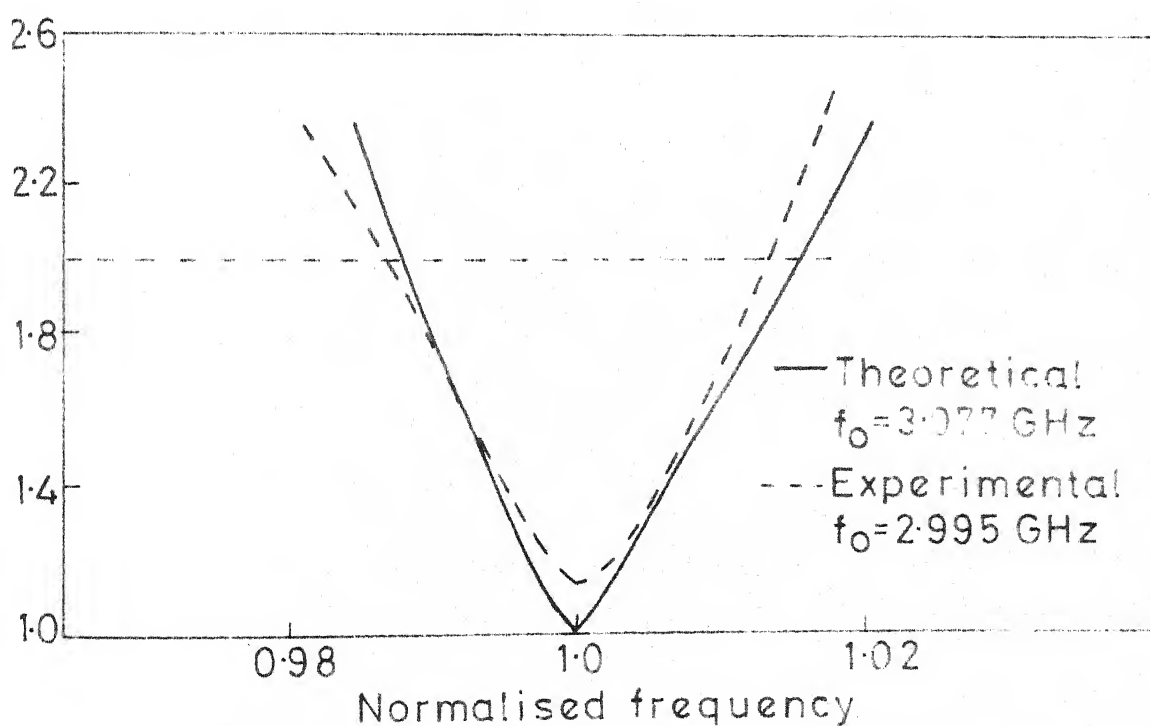


Fig.3.12 Theoretical and experimental variations of input VSWR with normalised frequency

be along the diagonal. Hence, several feed-ports are considered along the diagonal (near the shorted edges) as shown in Fig. 3.11(b) and the feed-location at which point input impedance is 50 ohms is obtained at $l = 0.65$ cm. Bandwidth and radiation pattern are calculated as discussed in earlier cases.

3.4.2 Bandwidth

Theoretical and experimental variations of input VSWR with normalized frequency are plotted in Fig. 3.12. The calculated and measured bandwidths are 83 MHz (2.7 percent, centre frequency $f_o = 3.077$ GHz) and 77 MHz (2.6 percent, centre frequency $f_o = 2.995$ GHz) respectively. The calculated bandwidth of a rectangular patch antenna with open boundary operating at same centre frequency is around 3.5 percent. It is noted that bandwidth is less in the short-circuited case compared to open-boundary case.

3.4.3 Radiation pattern

In this case, the maximum radiation is along the diagonal. So, the radiation field components E_θ and E_ϕ are calculated in $\phi = 45^\circ$ and $\phi = 135^\circ$ planes. It is noted that only E_ϕ is present in $\phi = 45^\circ$ plane, whereas only E_θ is present in $\phi = 135^\circ$ plane. The theoretical and experimental variations of radiation field components E_ϕ (in $\phi = 45^\circ$ plane) and E_θ (in $\phi = 135^\circ$ plane) are plotted in Figs. 3.13(a) and (b). The

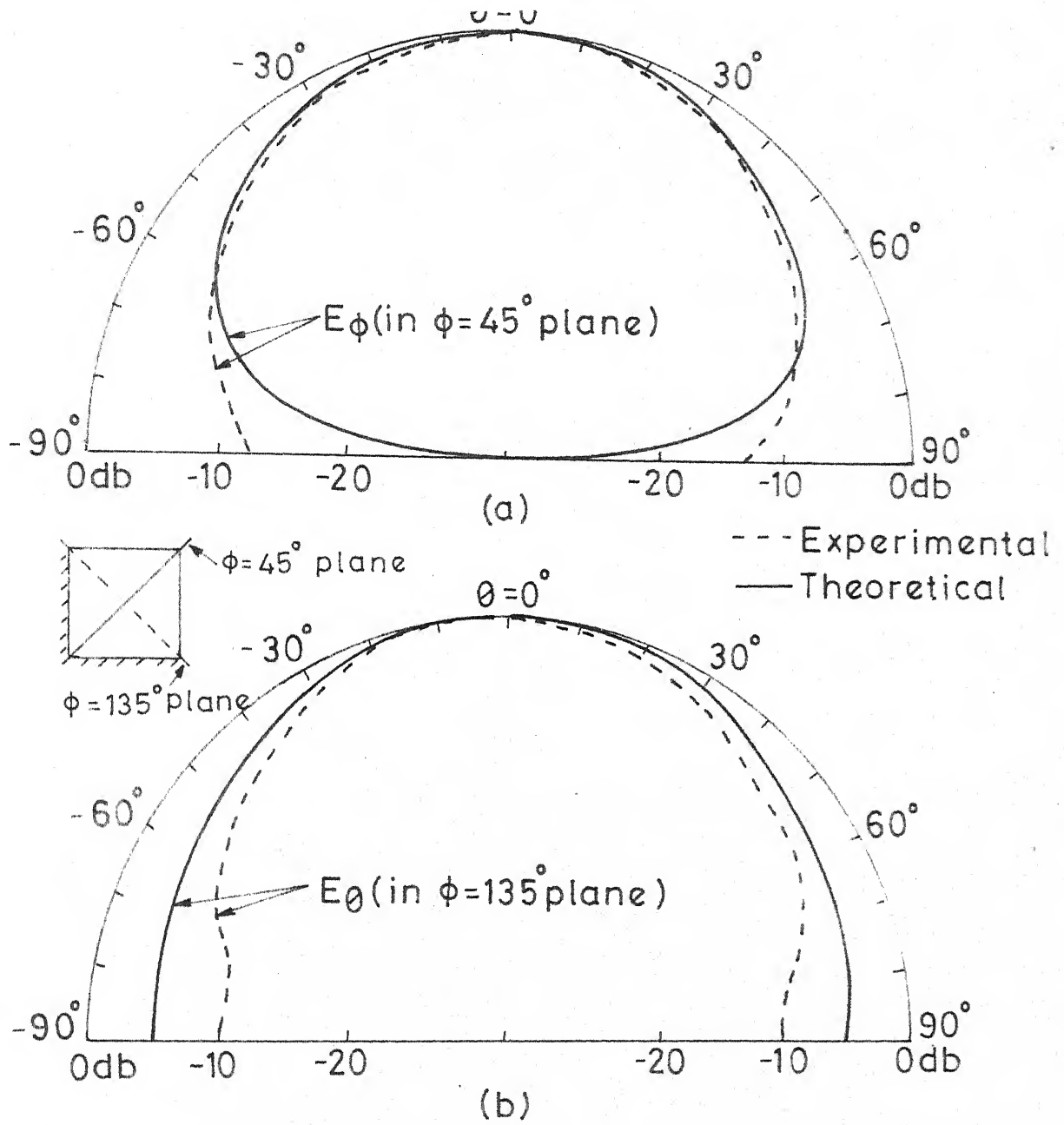


Fig. 3.13 Theoretical and experimental radiation patterns (a) E_ϕ in $\phi = 45^\circ$ plane (b) E_θ in $\phi = 135^\circ$ plane of a square patch antenna with two adjacent sides as electric wall shown in Fig. 3.11(a)

theoretical 3-db beamwidths in $\varphi = 45^\circ$ and $\varphi = 135^\circ$ planes are 88° and 95° respectively. The corresponding measured beamwidths are 76° and 75° respectively.

3.5 RECTANGULAR PATCH ANTENNA WITH THREE SIDES AS ELECTRIC WALLS

3.5.1 Analysis

The Green's function of a rectangle with three sides as electric walls given in (2.38) is used for analysis and is written as

$$G(x, y/x_0, y_0) = \frac{j \omega \mu d}{ab} \sum_{m=-\infty}^{\infty} \sum_{n=-\infty \atop \text{odd}}^{\infty} \frac{\sin(k_x x_0) \sin(k_y y_0) \sin(k_x x) \sin(k_y y)}{(k_x^2 + k_y^2 - k^2)} \quad (3.17)$$

$$\text{where } k_x = \frac{m\pi}{a} \text{ and } k_y = \frac{n\pi}{2b}$$

The resonant frequency for any mode can be obtained from

$$f = \frac{1}{2\pi} \sqrt{\frac{1}{\mu\epsilon} \left[\left(\frac{m\pi}{a}\right)^2 + \left(\frac{n\pi}{2b}\right)^2 \right]} \quad (3.18)$$

where a and b are effective length and width of the rectangle.

A square patch antenna with three sides as electric walls of dimensions, length (L) and width (W) equal to 4.0 cm excited at $(1,1)$ mode as shown in Fig. 3.14(a) is analyzed. As there is no field at the three shorted edges, the effective length is taken same as physical length and for finding effective width, extension is considered at one side (open-end) and is obtained as 4.28 cm. No ports are considered along the shorted edges. Several feed-ports are considered along the open-edge as shown in Fig. 3.14(b) and the feed-location,

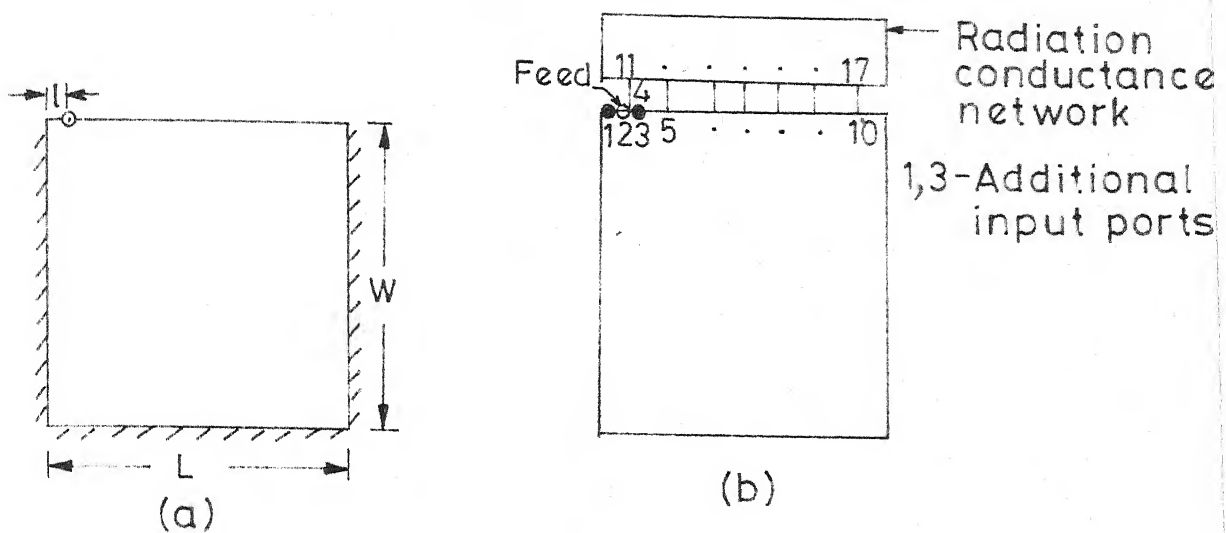


Fig. 3.14 (a) Square patch antenna with three sides as electric walls
 (b) its segmented network

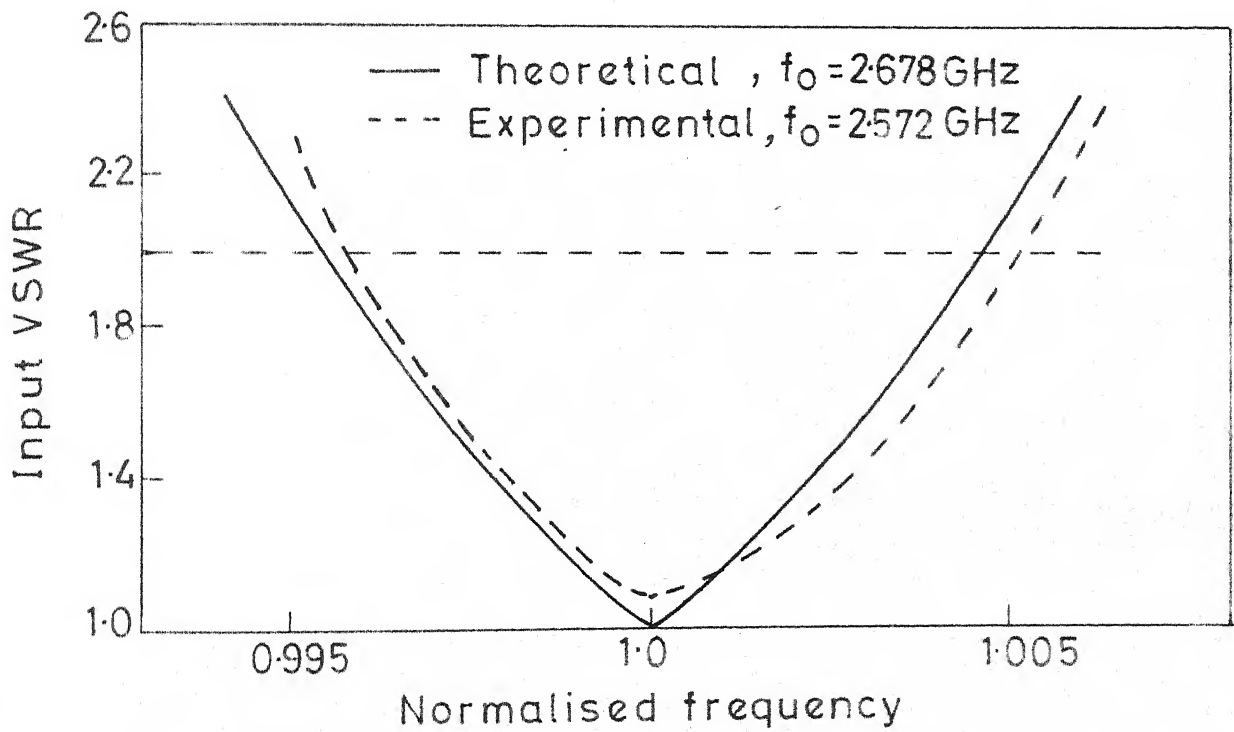


Fig. 3.15 Theoretical and experimental variations of input VSWR with normalised frequency

where input impedance is 50 ohms for (1,1) mode is obtained at $\ell = 0.32$ cm. Analysis is carried out as in the earlier cases.

3.5.2 Bandwidth

Theoretical and experimental variations of input VSWR with normalised frequency are shown in Fig. 3.15. The calculated bandwidth is 24 MHz (0.39 percent, centre frequency $f_0 = 2.678$ GHz). The measured bandwidth is 23 MHz (0.895 percent, centre frequency $f_0 = 2.572$ GHz). This bandwidth is very less compared to that of open-boundary rectangular micro-strip antenna.

3.5.3 Radiation pattern

Radiation field components E_θ and E_ϕ are calculated in $\varphi = 0^\circ$ and $\varphi = 90^\circ$ planes. It is noted that only E_ϕ is present in $\varphi = 0^\circ$ plane whereas only E_θ is present in $\varphi = 90^\circ$ plane, which is reverse of the rectangular patch antenna with open-boundary case. This is due to the fact that in this case the radiation is from the only open-edge, where the field varies sinusoidally, whereas most of the radiation in open-boundary case is from the edges where the field is maximum and constant. This is the cause of lower bandwidth also.

Theoretical and experimental variations of E_ϕ in $\varphi = 0^\circ$ plane and E_θ in $\varphi = 90^\circ$ plane are plotted in Figs. 3.16(a)

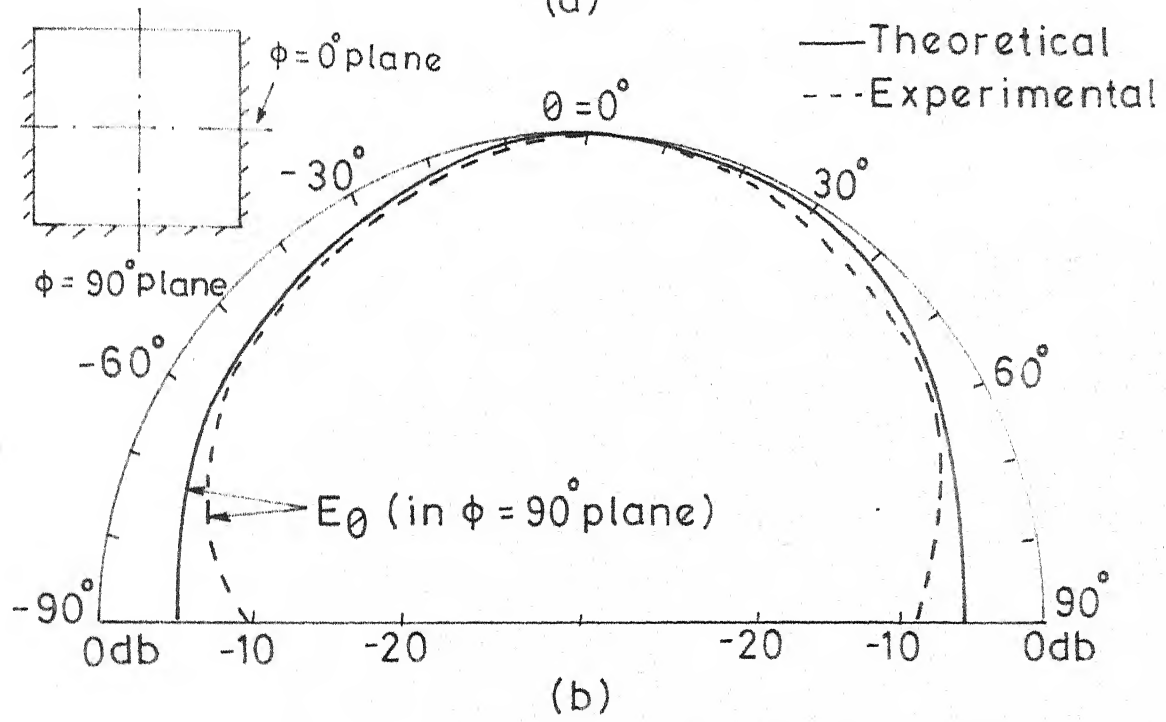
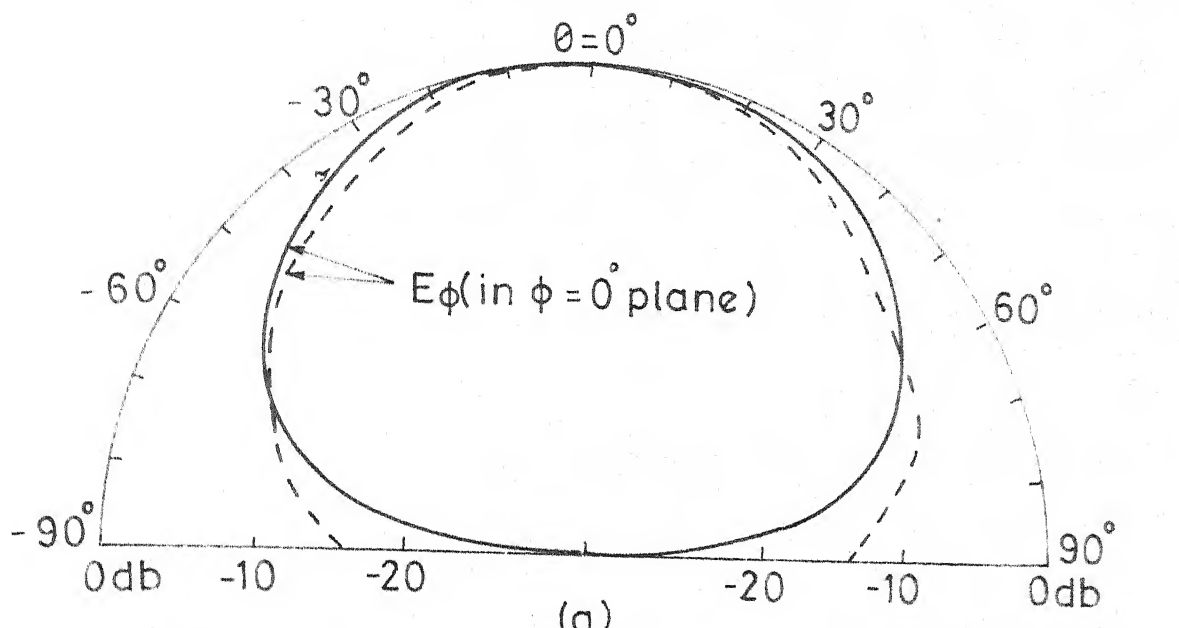
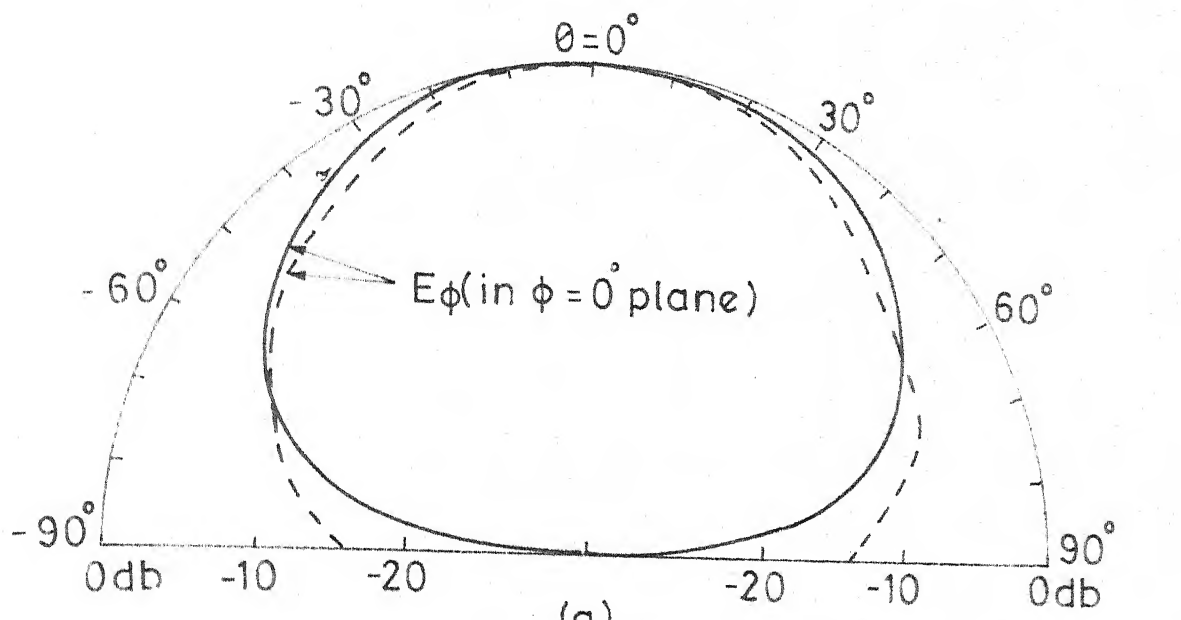
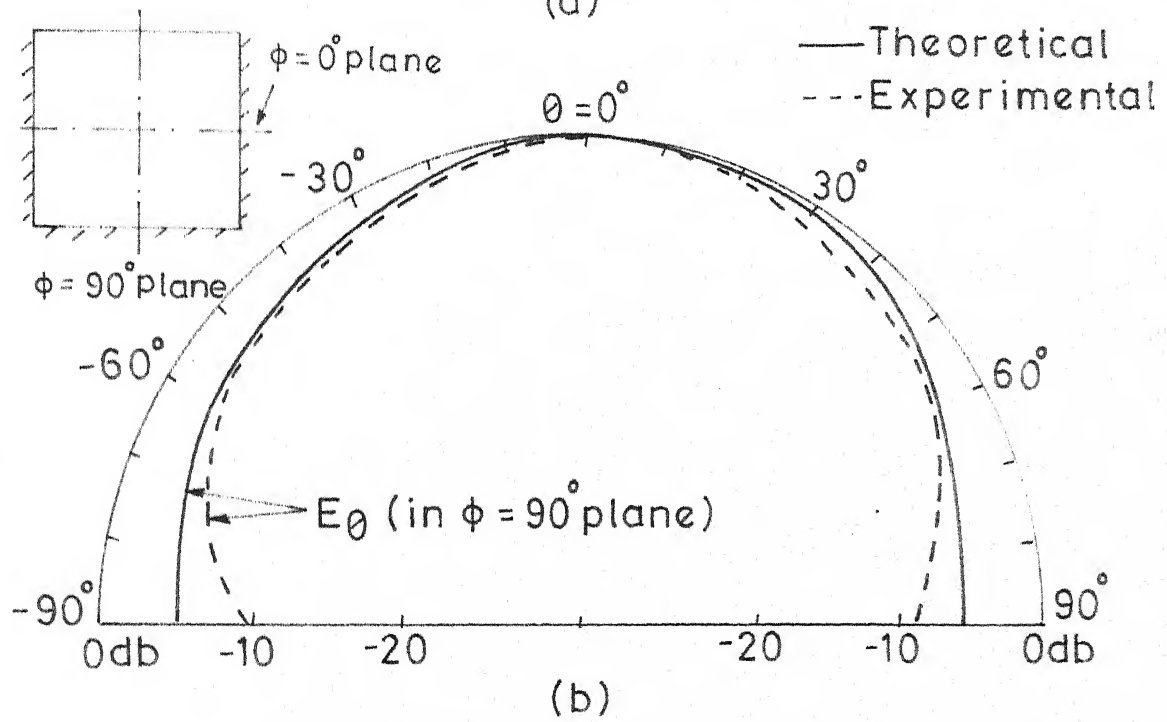


Fig.3.16 Theoretical and experimental radiation patterns (a) E_ϕ in $\phi = 0^\circ$ plane and (b) E_θ in $\phi = 90^\circ$ plane of a square patch antenna with three sides as electric walls shown in Fig. 3.14(a)



(a)



(b)

Fig.3.16 Theoretical and experimental radiation patterns (a) E_ϕ in $\phi=0^\circ$ plane and (b) E_θ in $\phi=90^\circ$ plane of a square patch antenna with three sides as electric walls shown in Fig. 3.14(a)

and (b). The theoretical 3-db beamwidths in $\varphi = 0^\circ$ and $\varphi = 90^\circ$ planes are 85° and 105° respectively. Corresponding measured beamwidths are 70° and 95° respectively. These beamwidths are more than the beamwidths of the rectangular patch antenna with open-boundary case.

3.6 MEASUREMENT OF MUTUAL COUPLING BETWEEN ONE-SIDE SHORTED RECTANGULAR MICROSTRIP ANTENNAS

3.6.1 Introduction

Microstrip antenna arrays have found wide applications in recent years and have inherent advantages such as light weight, low cost, relative ease of construction, and either conformability to the mounting surface or, at least, an extremely thin protrusion from the surface. These arrays have been mainly used wherever high gain and pattern shaping are required. Microstrip arrays are limited in that they tend to radiate efficiently only over a narrow band of frequencies and they cannot operate at the high power levels of waveguide, coaxial line, or even stripline.

In general, when a well matched individual element is placed in an array environment, its terminal properties will change due to mutual coupling effects. These mutual coupling effects may cause increased sidelobe levels, main beam squint, grating lobes, filled or shifted nulls and array blindness at some scan angles. However, mutual coupling can produce an improvement in side lobe levels for

those cases where the coupling causes a further tapering of the array distribution function. It would therefore be of substantial value to be able to predict coupling effects on microstrip array performance.

Mutual coupling between L-band rectangular, nearly square and circular microstrip antennas with open-boundary have been investigated experimentally by a series of measurements of the S-parameters [21]. Mutual coupling depends on element spacing, substrate thickness and patch size. The mutual coupling level decreases monotonically with increasing separation between elements and increases with the increase in the thickness of the substrate and patch size. For rectangular patches with 0.318 cm substrate thickness, E-plane and H-plane coupling values are -17 dB to -28 dB and -18 dB to -50 dB respectively, for element spacing range $0.15\lambda - 1.25\lambda$. For same spacing range, the E-plane and H-plane coupling values for nearly square patch antennas are -18 dB to -28 dB and -10 dB to -40 dB respectively. The H-plane coupling values are more in the case of nearly square patch antennas due to increased H-plane radiation and hence there is a crossover in the E- and H-plane curves.

In this section, an experimental study of mutual coupling between one-side shorted rectangular microstrip antennas has been carried out.

3.6.2 Experimental technique and results

The S-parameters are measured with a network analyzer system. The measurements are made on a two element array as a function of element spacing. The isolated elements are designed to operate with an approximate 50 ohms input impedance at resonance. The S_{ii} are measured as the reflection coefficient seen at one port while the other port is terminated in a 50 ohms load. The S_{ij} ($i \neq j$), which give mutual coupling between elements are measured as the transmission coefficient between the ports when a 50 ohms source is connected at one port and a 50 ohms detector is placed at the second port.

Two-element arrays (with E-plane coupling) of one-side shorted rectangular microstrip antennas as shown in Fig.3.17, are fabricated on copper-cladded 0.318 cm thick polystyrene substrate of relative permittivity 2.55 for two spacings. The individual elements of array are designed to operate at 2.10 GHz with an approximate input impedance of 50 ohms.

For 0.3λ and 0.6λ spacings, the values of $|S_{21}|^2$ obtained are -21 dB and -28 dB respectively (values of $|S_{12}|^2$ being almost same). The input impedance loci for the coupled case ($S = 0.3\lambda$) and for an individual element (i.e. uncoupled) are plotted in Fig. 3.19. The coupled locus encloses the uncoupled locus, whereas in case of open-boundary rectangular microstrip antennas the uncoupled impedance locus encloses the coupled locus [22].

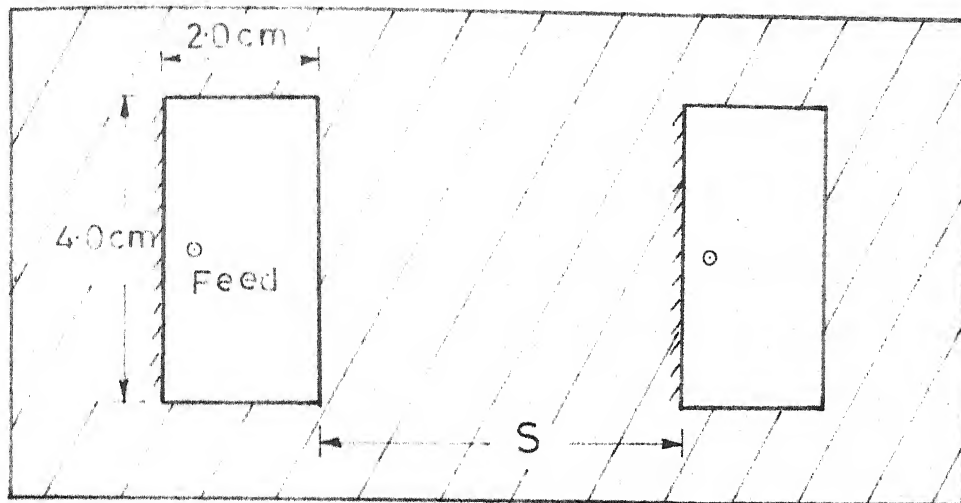


Fig.3.17 Two element array of one side short-circuited rectangular microstrip antennas

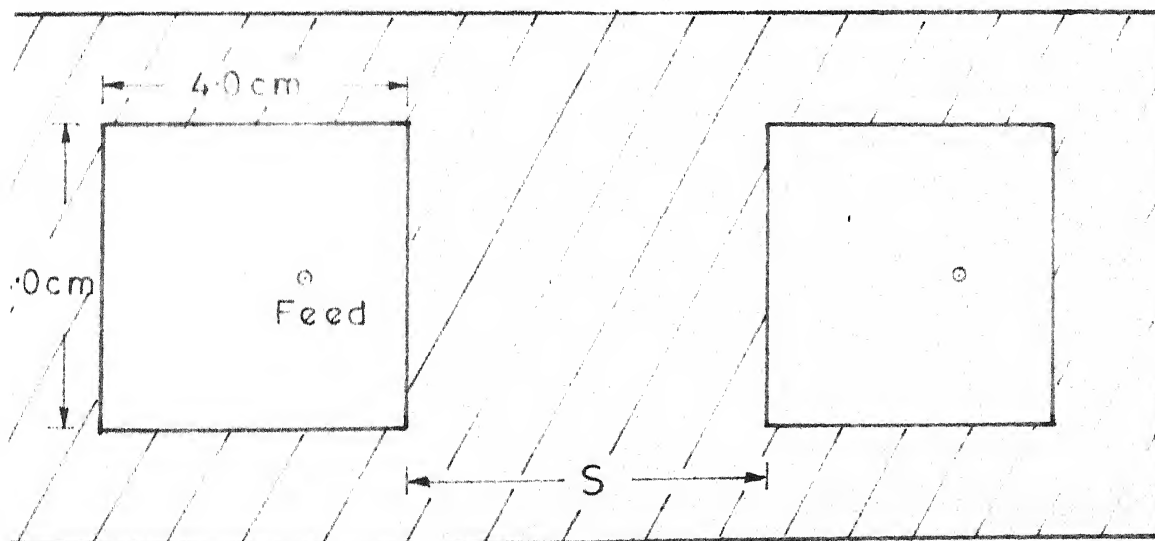


Fig.3.18 Two element array of open-boundary square microstrip antennas

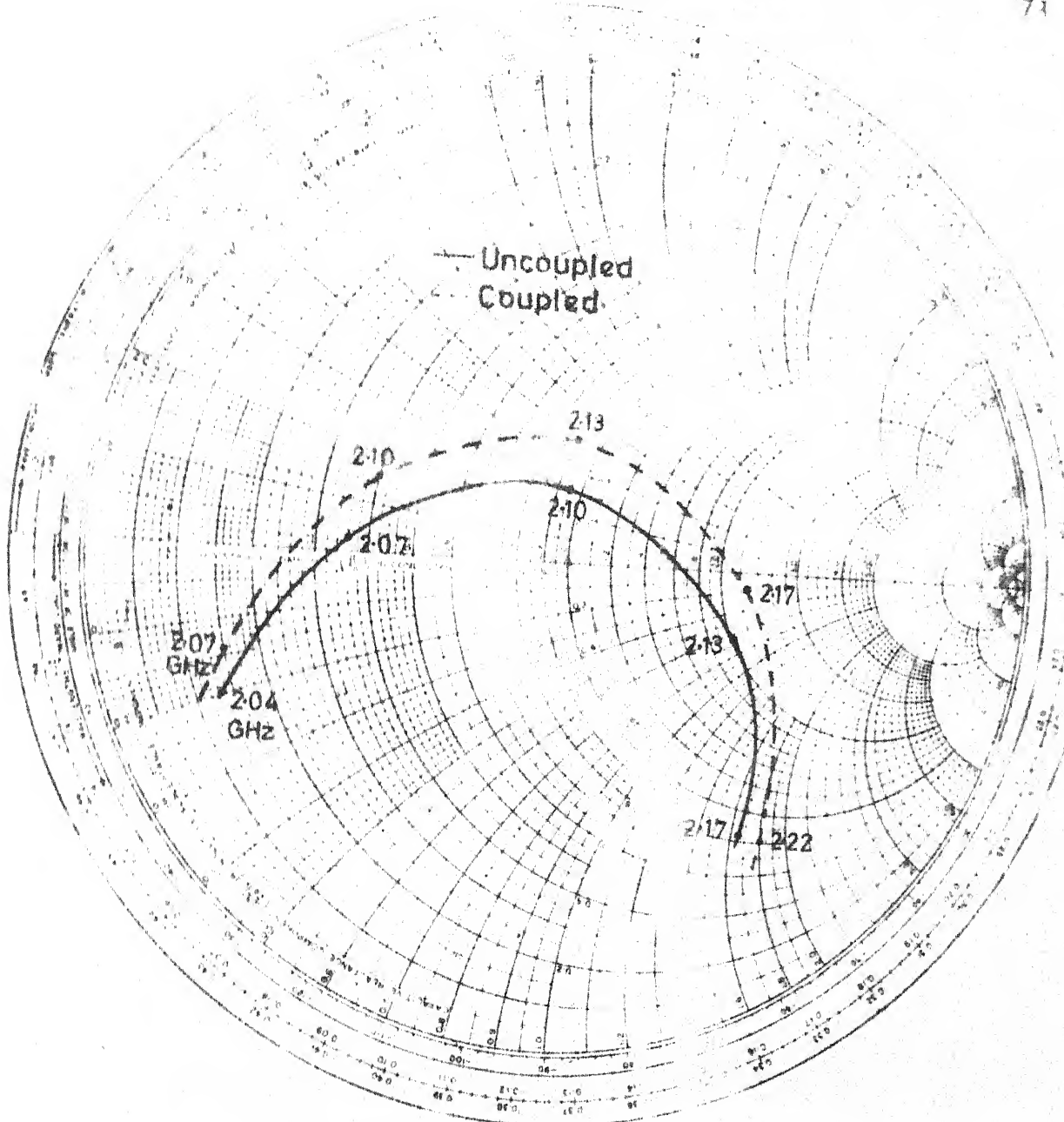


Fig. 3.19 Input impedance loci for coupled ($S = 0.3\lambda$) and uncoupled (centre frequency = 2.10 GHz) one side short-circuited rectangular microstrip antennas

For comparison purpose, two-element arrays of open-boundary square microstrip antennas as shown in Fig.3.18 are fabricated. In this case, the measured values of $|s_{21}|^2$ are -19 dB and -25.5 dB respectively for 0.3λ and 0.6λ spacings. It is noted that mutual coupling is less for one-side shorted rectangular microstrip antennas as compared to open-boundary antennas.

Chapter Four

CONCLUDING REMARKS

This chapter contains summary of the results reported in this thesis and some suggestions for further investigations.

4.1 SUMMARY OF RESULTS

The investigations reported in this thesis can be divided into two categories - (i) derivations of Green's functions for mixed boundary 2-d planar segments and (ii) their applications to microstrip antennas.

The method of images has been employed to obtain the eigen functions of the Helmholtz equation, which are then used to derive the Green's functions. Green's functions of mixed boundary planar segments for the following cases have been derived.

- (a) rectangular segment with
 - i) two adjacent sides as electric walls,
 - ii) two parallel sides as electric walls,
 - iii) three sides as electric walls,
 - iv) electric wall boundary and
- (b) isosceles right-angled triangular segments with
 - i) hypotenuse and one of the other sides as electric walls,
 - ii) hypotenuse as magnetic wall and other two sides as electric walls,
 - iii) electric wall boundary.

Green's function approach for the analysis of two-dimensional components has been used for analyzing mixed boundary rectangular microstrip antennas. The various antennas studied are : Rectangular microstrip antenna with (i) one side as an electric wall, (ii) two adjacent sides as electric walls and (iii) three sides as electric walls.

From the theoretical and experimental studies of mixed boundary rectangular antennas, the following observations are made :

- i) Size of these antennas are less compared to those of the open-boundary antennas for the same operating frequency .
- ii) Bandwidth of these antennas are less compared to open-boundary antennas and the bandwidth decreases as the number of shorted edges are increased .
- iii) Beamwidths are more than those of the open-boundary antennas .
- iv) Mutual coupling between the elements is less as compared to the open-boundary antennas, as observed in the case of one-side shorted rectangular antennas.

4.2 SUGGESTIONS FOR FURTHER INVESTIGATIONS

In shorted boundary rectangular and isosceles right-angled triangular resonators (for which Green's functions

are derived), radiated power is zero and hence Q-factor is high. So, their applications as high-Q resonators can be studied.

Detailed study of mutual coupling in the cases of one-side shorted and two adjacent sides shorted rectangular antennas can be carried out.

When the element size is a limiting factor, as in phased arrays, where lot of space is required for phase shifters, corporate feed and bias lines, one-side shorted rectangular antennas can be used. The size of these antennas are half of the open-boundary antennas, as these are quarter-wave antennas. Mutual coupling between the elements is less and bandwidth is reduced by only 9 percent as compared to open-boundary rectangular antennas. Therefore, a detailed study of phased arrays with one-side shorted rectangular antennas can be carried out.

REFERENCES

- [1] T. Okoshi and T. Miyoshi, 'The planar circuit - An approach to microwave integrated circuitry', IEEE Trans. Microwave Theory Tech., vol. MTT-20, pp 245-252, April 1972.
- [2] T. Okoshi and T. Takeuchi, 'Analysis of planar circuits by segmentation method', Electron. Commun. Japan, vol. 58-B, No.8, pp 71-79, Aug. 1975.
- [3] T. Okoshi, Y. Uehara, and T. Takeuchi, 'The segmentation method - An approach to the analysis of microwave Planar Circuits', IEEE Trans. Microwave Theory Tech., vol. MTT-24, pp 662-668, Oct. 1976.
- [4] T. Okoshi, T. Takeuchi, and J.P. Hsu, 'Planar 3-db hybrid circuit', Electron. Commun. Japan, vol. 58-B, No.8, pp 80-90, Aug. 1975.
- [5] R. Chadha and K.C. Gupta, 'Green's functions for triangular segments in planar microwave circuits', IEEE Trans. Microwave Theory Tech., vol. MTT-28, pp 1139-1143, Oct. 1980.
- [6] R. Chadha and K.C. Gupta, 'Green's functions for circular sectors, annular rings and annular sectors in planar microwave circuits', IEEE Trans. Microwave Theory Tech., vol. MTT-29, pp 68-71, Jan. 1981.
- [7] P.C. Sharma, 'Desegmentation method and its application to circularly polarized microstrip antennas', Ph.D. Thesis, Department of Electrical Engineering, Indian Institute of Technology, Kanpur, India, Apr. 1982.
- [8] P. Silvester, 'Finite element analysis of planar microwave networks', IEEE Trans. Microwave Theory Tech., vol. MTT-21, pp 104-108, Feb. 1973.
- [9] K.C. Gupta, R. Garg, and I.J. Bahl, Microstrip Lines and Slotlines, Dedham, MA: Artech House, 1979.
- [10] K.C. Gupta and P.C. Sharma, 'Segmentation and desegmentation techniques for analysis of planar microstrip antennas', IEEE AP-S Int. Symp. Digest, pp 19-22, June 1981.

- [11] I.J. Bahl and P. Bhartia, *Microstrip antennas*, Dedham, MA: Artech House, 1981.
- [12] R.E. Munson, 'Conformal microstrip antennas and arrays', *IEEE Trans. Antennas Propagat.*, vol.AP-22, pp 74-78, Jan. 1974.
- [13] Y.T. Lo, D. Solomon and W.F. Richards, 'Theory and experiments on microstrip antennas', *IEEE Trans. Antennas Propagat.*, vol.AP-27, pp 137-145, March 1979.
- [14] K.R. Carver and E.L. Coffey, 'Theoretical investigation of the microstrip antenna', New Mexico State Univ., Tech. Rep. PT-00929, Jan. 1979.
- [15] J.H. Richmand, 'A wire-grid model for scattering by conducting bodies', *IEEE Trans. Antennas Propagat.*, vol.AP-14, pp. 782-786, Nov. 1966.
- [16] H.M. Altschuler and A.A. Oliner, 'Discontinuities in the center conductor of symmetric strip transmission line', *IRE Trans. Microwave Theory Tech.*, vol.MTT-8, pp 328-339, May 1960.
- [17] P.M. Morse and H. Feshbach, *Methods of Theoretical Physics*, New York: McGraw-Hill, 1953, Ch. 7.
- [18] R. Chadha, 'Triangular segments and two-dimensional analysis for microwave integrated circuits', Ph.D. Thesis, Department of Electrical Engineering, Indian Institute of Technology, Kanpur, India, May 1981.
- [19] I. Wolff and N. Knoppik, 'Rectangular and circular microstrip disc capacitors and resonators', *IEEE Trans. Microwave Theory Tech.*, vol. MTT-22, pp 857-863, Oct. 1974.
- [20] H. Pues and A. Van de Cappelle, 'A simple accurate formula for the radiation conductance of a rectangular microstrip antenna', *IEEE AP-S Int. Symp. Digest*, pp 23-26, June 1981.
- [21] R.P. Jedlicka, M.T. Poe and K.R. Carver, 'Measured mutual coupling between microstrip antennas', *IEEE Trans. Antennas Propagat.*, vol. AP-29, pp 147-149 , Jan.1981.
- [22] C.M. Krown, 'E-plane coupling between two rectangular microstrip antennas', *Electronics Letters*, vol. 16, pp 635-636, July 31, 1980.